ABSTRACT

Title of Thesis: STUDIES OF ENCAPSULATION BY SORPTION, CHARACTERIZATION, AND RELEASE OF ANTI-CANCER DRUG 6-THIOGUANINE FROM ALUMINUM METAL-ORGANIC FRAMEWORK BASOLITE A100

Cole Grinnell, M.S. December 2019

Thesis Chair: Alexandr Samokhvalov, PhD
Department of Chemistry

Metal-organic frameworks (MOFs) have already gained prominence in materials science research due to their high loading capacity and structural variability. Initial research showed the capabilities being used toward applications like gas sequestration, but contemporary investigations have shown a wider variety of uses, such as drug encapsulation and release. The MOF Basolite A100 (A100), with its relatively high biocompatibility, moderate pore size and plentiful commercial availability, was selected to further look in to the use of MOFs as a drug delivery platform. For a model drug, the anti-cancer compound 6-Thioguanine (6-TG) was chosen for its molecular size, novelty and use in therapeutic treatments compatible with MOF delivery. This thesis will show a method toward the encapsulation of 6-TG using dimethyl sulfoxide (DMSO) as solvent, and characterize the resultant complex A100-DMSO-6TG via X-ray diffraction (XRD), fluorescence spectroscopy and differential scanning calorimetry (DSC). In addition, the release kinetics of the 6-TG from two different forms of the complex in a

phosphate buffer saline (PBS) were studied via high performance liquid chromatography (HPLC). It was observed that 6-TG resides in two locations in the cavity of A100 and forms bonds both directly between itself and the A100 as well as through the DMSO molecule to the A100. This results in an initial quick release of the surface bound 6-TG and the secondary release of the 6-TG from the cavity, a process slowed by pelletizing. Chemical kinetics of delayed release suggests a future potential therapeutic use based on initial cytotoxicity followed by growth inhibition, with much room for future studies along this axis.

STUDIES OF ENCAPSULATION BY SORPTION, CHARACTERIZATION, AND RELEASE OF ANTI-CANCER DRUG 6-THIOGUANINE FROM ALUMINUM METAL-ORGANIC FRAMEWORK BASOLITE A100

by

Cole Grinnell

A Thesis Submitted in Partial Fulfillment

of the Requirements for the Degree

Master of Science

Morgan State University

December 2019

STUDIES OF ENCAPSULATION BY SORPTION, CHARACTERIZATION, AND RELEASE OF ANTI-CANCER DRUG 6-THIOGUANINE FROM ALUMINUM METAL-ORGANIC FRAMEWORK BASOLITE A100

by

Cole Grinnell

has been approved

December 2019

THESIS COMMITTEE APPROVAL:

_____, Chair

Alexandr Samokhvalov, PhD

_____

Fasil Abebe, PhD

_____

Yongchao Zhang, PhD

Acknowledgments

A deep thanks to my advisor Dr. Alexandr Samokhvalov, who helped tie all the pieces together and helped encourage me that all this was well within my doing.

Many thanks to the support and patience of my fellow staff and faculty in the Department of Chemistry, with special mention of Dr. Solomon Tadesse for his technical assistance and generous lending of time.

Much love to my family for their support and affection through this very long process and for making me the kind of person to be able to do this today.

Additional thanks to Ms. Sonia Scott for help with archival access for my background material and Ms. Thea Climento for Dutch translation assistance.

I would like to thank the staff of the Station North Tool Library for their assistance with the many small fabrication jobs associated with my research.

I would also like to thank the staff of the Peabody Heights Public Space for their hospitality during their stint as my writing room.

Table of Contents

List of Tables

List of Figures

1 Introduction

1.1 Metal-organic frameworks (MOFs)

Seen as an outgrowth of research into porous materials that started with zeolites[1] and advanced through certain coordination polymers[2], metal-organic frameworks (MOFs) have been at the forefront of demonstrating the numerous advantages of high surface area compounds. Beginning with the discovery and characterization of MOF-5[3], the past 2 decades have seen MOF research expand toward a multitude of applications. This versatility of application is in many ways linked to a versatility in the structure of MOFs themselves. At their core, MOFs are coordination complexes between metal ion centers and organic linkers[4]. They are synthesized by solvo- or hydrothermal means from solutions containing metal salts, di- and tricarboxylic acids and solvents[5]. As pressure is increased in the reaction chamber, bonds form between the carboxylic acid groups in the linkers and the metal ions.[6] The metal ions also act as secondary building units (SBUs), with their coordination geometries influencing numerous factors which affect MOF's structure and properties.[7] Figure 1 shows formation and structure of one of the benchmark metal-organic framework, MOF-5.

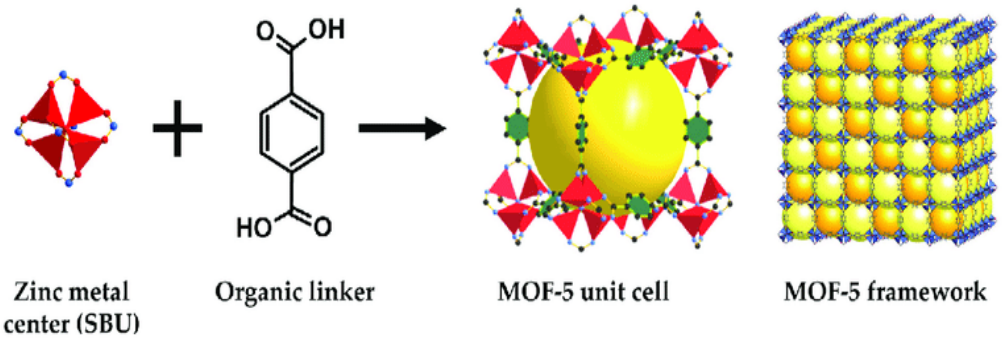

Figure 1. MOF-5 synthesis (Edson V. Perez, Chamaal Karunaweera, Inga H. Musselman, Kenneth J. Balkus and John P. Ferraris , Processes, 2016, 4, 32 DOI: 10.3390/pr4030032 Reproduced by permission under a Creative Commons Attribution Non-Commercial 3.0 Unported License)

The numerous combinations of the SBU's and organic linkers can lead to a high variety of different shapes and sizes of the entrance into the MOF (pores) and to the chemical environment and area of the interior of the same pore[8]. This allows MOFs to have a diversity of structures originating from a relatively small set of initial reagents and allows a high degree of tunability in the final material, with predictable topologies related to SBUs generating narrow ranges of pores and cavities that can be selected for. Once these structures are formed the solvent is evacuated, clearing the pores and allowing access to the MOF's high surface area for the hosting of different molecules dependent on application[9].

1.2 Aluminum MOFs

One subset of interest would be MOFs based on aluminum SBUs. The resultant MOFs are somewhat smaller in pore size and surface area than those formed by some other metals. They also possess a high thermal and chemical stability in a variety of environments as well as the certain amount of structural variability, and possess the

ability to encapsulate smaller molecules[10]. In addition, aluminum-based MOFs (Al-MOF) are relatively benign, environmentally speaking (particularly when compared to MOFs based on toxic metals such as chromium), which opens Al-MOFs to applications which are more sensitive to "green" concerns like pollution control[11] or biomedical usage[12].

One Al-MOF of interest, seen in Figure 2, is one based on the organic linker of benzenedicarboxylic acid (BDC) and aluminum hydroxide, known as MIL-53(Al). MIL-53(Al) with a bulk density of ≈ 0.4 g/cm^3 and a Brunauer–Emmett–Teller (BET) surface area of $\approx$1200 m^2/g [13], displays the smaller size and resiliency mentioned above. It is a well characterized material with a production scalable enough, so it is one of a few Al-MOFs to be produced commercially by BASF[14] as Basolite A100. This availability allowed the research to side step the problems of the in-lab synthesis, while more closely mirroring how this MOF might be used in a non-academic setting.

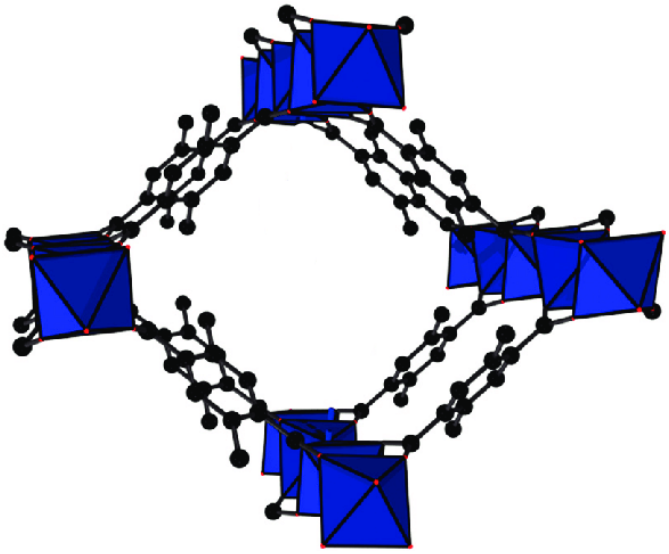

Figure 2. Structure of MIL-53 (T. Homburg, C. Hartwig, H. Reinsch, M. Wark and N. Stock, *Dalton Trans*., 2016, **45**, 15041 **DOI**: 10.1039/C6DT03048C. Reproduced from the Royal Society of Chemistry by permission under a Creative Commons Attribution Non-Commercial 3.0 Unported License)

1.3 MOF functionality

Initially, this tunable function of sorbents was applied to the separation and sequestration of mixtures of gases[15]. However, advances in MOF synthesis and post-synthetic modification (PSM) have opened up many more applications. These include clean fuel technology, environmental remediation, food science and catalysis[16]. Research into the use of MOFs in biomedicine has also greatly expanded in recent years, and it is in this area that my research hopes to occasionally see an applicability. The high internal surface area gives MOFs a high carrying capacity for pharmaceutical drugs[17], and their large pore size allows them to carry drug molecules too large to fit pores in other materials[18]. Once encapsulated in a MOF, the drugs

have been shown to be more protected from background metabolic processes and hydrolysis, preserving more molecules to reach the therapeutically affected area upon their subsequent release[19]. This tunability of MOFs (through SBU selection and post-synthetic modification) can allow for more targeted release[20], with certain metals acting as Lewis acid sites for smaller biomolecules associated with certain regions of the body[21] and with organic linkers modified with certain functional groups to allow them to interface better with specific membranes[22]. An additional benefit from protection and targeted release of bioactive molecules by MOFs is seen in relation to drug molecules for cancer chemotherapy. These chemotherapeutic drugs, while being designed to target cancer cells, and particularly cancer cells of certain tissues and organs, regrettably do not have perfect selectivity in their cytotoxic action and may negatively impact cells across the body resulting in symptoms commonly associated with side effects[23]. The MOFs, which are effective in both isolating anti-cancer drugs from the rest of the body en route to targeted cells[24], but also releasing their encapsulated cargo in therapeutic amounts at the site where it is needed, could reduce the negative side effects correlated with chemotherapy treatments[24].

1.4 Anti-cancer drug 6-Thioguanine

Due to the moderate pore size of Basolite A100 (A100), only smaller drug molecules were under consideration to test encapsulation and delivery efficacy of A100, with anti-cancer drugs being of particular interest due to reasons stated in Section 1.3. The drug 6-thioguanine (6-TG) was selected as it has those attributes, in addition to being well characterized[25], widely available[26] and FDA-approved. This

drug could benefit from a host material/carrier, which would increase its availability through its journey to the bloodstream. 6-TG is from anti-metabolite family of drugs[27] that includes the benchmark purine guanine, which disrupts DNA transcription[28]. 6-TG has molecular weight of 167.19 g/mol and is used as a treatment for several forms of leukemia, or cancers afflicting blood cell formation tissues in bone marrow[27]. Being a purine based molecule, 6-TG may have good interactions with cyclic fragments in organic linkers in A100 and form the π-π stacking[29]. When 6-TG medication is taken orally, it takes approximately 8 hours for it to reach the maximum concentration in blood plasma, and it has a half-life in plasma of, on average, 80 minutes before being metabolized to nucleotides[26].

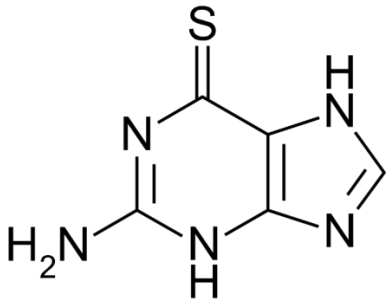

Figure 3. Molecular structure of 6-TG

1.5 Dimethyl sulfoxide, drug encapsulation and release

There are several means by which a molecule might be encapsulated into a MOF. While there exists an early work in using mechanical action to "grind" drugs into the complex[30], most efforts use the means of a solvent. This can occur as a "one-pot" method, where the drug is dissolved in the same solution containing the metal salt and organic acid, and MOF synthesis and drug encapsulation occur simultaneously[31].

However, as commercial availability was one of the aspects that drew this research toward Basolite A100 (also denoted as A100 in this Thesis), drug encapsulation will need to occur as a separate, second step from synthesis[32]. As A100 is essentially insoluble in any solvent, the solubility of 6-TG would be the determining factor in solvent selection, particularly as 6-TG itself has a very low solubility in water[27]. Solubility data for non-water, non-alkaline solutions were spare and sometimes contradictory, but it was determined that dimethyl sulfoxide (DMSO) should serve this purpose well. DMSO is thermally stable at biologically relevant temperatures and fully miscible in the aqueous solutions that comprise living tissue[33]. In addition, compared to many similar polar aprotic solvents, DMSO has a much lower toxicity and itself has numerous medical uses, particularly as a solvent of drug molecules applied as a topical treatment[33]. There were no prior experimental studies that showed any Al-MOF absorbing or desorbing DMSO. The only reported study of the sorption of DMSO on a MOF is a computation study conducted with zinc MOFs[34].

Initially, the kinetics of release of the encapsulated drugs was studied by the common method of periodic sampling of a large stirred media of standard phosphate buffer saline (PBS), which is selected to simulate the aqueous environment in human biological systems[35]. However, additional complications to this approach were noted in both low solubility of 6-TG in aqueous media and in the somewhat rapid metabolism in the bodily fluids through processes absent in PBS[36]. To better simulate this, it was proposed that the sample of solid complex "MOF/drug" should be periodically transferred to new portion of pure PBS, rather than samples are taken from the solution where the released drug would accumulate. In addition, while

therapeutic usage of 6-TG largely entails oral administration, other anti-metabolite drugs have been administered through implants[36]. To test the capability of A100 as a potential material for drug implantation, and to test release kinetics of 6-TG over longer time periods, the additional release experiments were planned using a pelletized version of complex “MOF/drug”.

1.6 MOF breathing effect

One characteristic of some MOFs, including A100, that relates to sorption and desorption is the so-called “breathing effect”. This effect describes the widening and narrowing of pore aperture in the MOF as host material during the incorporation and removal of the molecule (guest)[37]. Only a few MOFs exhibit the breathing effect, among them being MIL-53(Al) and its commercial equivalent Basolite A100[38]. When guest molecules form the hydrogen bonding with anions of dicarboxylic acids as organic linkers, pore changes from its “wide-pore” to a ”narrow-pore” state. When guest molecules are removed, these molecular interactions are broken, and the pore will return to a “wide-pore” state[39] as seen in Figure 4.

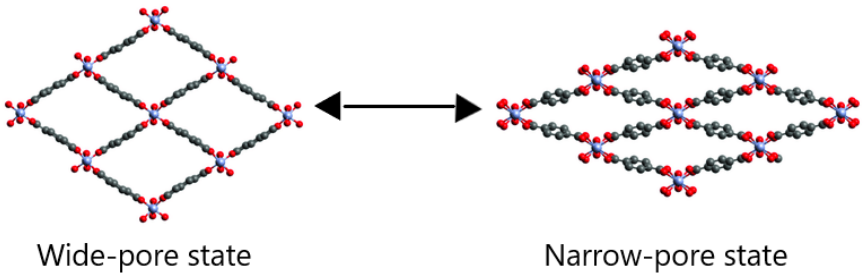

Figure 4. Structure of MIL-53 undergoing breathing effect (Weser, Oskar & Veryazov, Valera, *Frontiers in Chemistry*, (2017) **5**. 111. **DOI:** 10.3389/fchem.2017.00111. Reproduced from ResearchGate by permission under a Creative Commons Attribution 4.0 International License)

As this "wide-pore" state is more suitable for accepting guest molecules, most encapsulation procedures will include an "activation" step of applying heat and vacuum to fully remove any remaining organic precursors and water guest molecules. This renders the MOF ready, by returning it to a "wide-pore" state[40], for the subsequent sorption of guest molecules. As the shift from a "wide-pore" to "narrow-pore" state will alter the crystalline[41], electronic[42] and thermal[43] properties of a MOF that exhibits a breathing effect, qualitatively measuring these properties is one way of determining whether a guest molecule has successfully encapsulated into a given MOF.

1.7 Synchronous vs "conventional" fluorescence spectroscopy

In fluorescence spectroscopy, a monochromatically selected excitation wavelength of light (λ_{ex}) is shined to a substance, whose electrons are first excited to a higher electronic state and then relax back to the ground state and emit a "shifted"

wavelength of light (λ_{em}). When a monochromator "sweeps" this band of emitted light before it reaches a detector, it can be said that this fluorescence spectrometer is performing "conventional" emission spectroscopy. In addition, the λ_{em} can be held constant while the λ_{ex} is swept over a range of wavelengths. This would be the "conventional" excitation spectroscopy. While both "conventional" operation modes have many analytical uses, they face issues at room temperature with solid-state materials and particularly with complex solid materials like MOFs, namely they result in very broad peaks with low resolution and significant noise[44]. The complicated numeric analysis is needed to allow interpretation or, preferably, a substantially improved method of data collection is needed.

While in conventional fluorescence emission spectroscopy the λ_{ex} is held constant while the λ_{em} is swept over a range of wavelengths, in synchronous fluorescence spectroscopy one sweeps both the λ_{ex} and the λ_{em} (as the name would suggest) synchronized with each other[44]. The difference between the λ_{em} and λ_{ex} is held constant for the entire analysis, and it is referred to as $\Delta\lambda$. While there are few studies of synchronous fluorescence spectroscopy of solid-state materials[45], and none on MOFs prior to this work, it is a common technique to study solutions (i.e. the liquid phase) where it has demonstrated several benefits[44]. While the overall signal intensity at the detector is sometimes decreased, the peaks are significantly narrowed, noise is reduced, and solutions containing the multiple emitting substances ("fluorophores") can be successfully analyzed both qualitatively and quantitatively. Spectral peaks produced by the two (or more) fluorophores that emit at the similar wavelengths were

narrowed, whole the emission and excitation outside the given Δλ of interest are eliminated[46]. Since complexes of MOFs contain organic linkers, the absorbed organic compounds and metal cations[47], all of which can produce fluorescence under certain conditions, studies by synchronous fluorescence spectroscopy were planned to resolve the spectra of complex "MOF/drug" into the peaks from the individual fluorophores.

1.8 Modulated vs "conventional" differential scanning calorimetry

Differential scanning calorimetry (DSC) is used to detect physical and chemical changes in a material through changes in its heat capacity. A sample and a reference (usually an empty pan of the same material as the one holding the sample) are placed in a container being heated at the same rate, while each have their own temperature independently monitored. Many processes, notably including the conformation changes[43] and sorption/desorption[48] absorb or release a certain amount of heat. This change is detected as either an increase or decrease in the temperature of the sample compared to the reference. However, sometimes several changes in the material can occur over a small temperature range. Ordinarily, the corresponding peaks would be "obscured" under the somewhat board peaks and valleys in a "conventional" DSC scan. However, the DSC scan can be modulated when multiple cycles of heating and cooling are generated along the overall heating curve.

This modulated differential scanning calorimetry (MDSC), as seen above, introduces two new heat flows to the data. When a material has a change in the heat flow during the heating portion of the modulation cycle and then shows a

corresponding change in the heat flow in the opposite direction during the cooling portion of that same cycle, the process has a change in heat capacity and is defined as reversible[49]. On the other hand, the irreversible heat flow is unaffected by the modulated heating and cooling cycles. Processes with heat flow during heating cycle that does not occur during cooling cycle are irreversible[49]. MDSC is well suited to study complexes of MOFs and specifically Al-MOFs, as they can undertake both reversible and irreversible thermal changes over a narrow range of temperature. In particular, the change in the pore size would be a reversible process[43] whereas the desorption of guest molecules would be an irreversible process (as long as guest molecules are removed by the purge gas)[50]. Thus, MDSC could determine, among other properties, whether adsorption of drug molecules triggers the expected pore-changing breathing in the MOF.

1.9 Research Goals

The goal of this thesis is to study Al-MOF Basolite A100 as solid matrix for encapsulation by sorption in solution and the time-delayed release of anti-cancer drug 6-TG to the simulated biological fluid. The goal also includes characterization of the resultant complex (referred to as the ternary complex A100-DMSO-6TG for the remainder of this thesis) by the complementary methods of structural and spectroscopic analysis.

Chapter 1 will provide the background information on MOFs, the encapsulated drug and its encapsulation solvent, and several analytical techniques used to characterize them. Chapter 2 will consist of experimental description of the study

including the materials and chemicals used, descriptions of sample preparation, and experimental methods. Chapter 3.1 will discuss the characterization of the ternary complex A100-DMSO-6TG, while Chapter 3.2 will focus specifically on the characterization by fluorescence spectroscopy. Chapter 3.3 will speak about kinetics of delayed release of 6-TG from the complex. Finally, main conclusions of the study will be summarized in Chapter 4, along with avenues of future research suggested by the current work

2 Experimental

2.1 Materials

Basolite A100 (A100) is a commercially produced variant of MIL-53(Al) MOF which was purchased from Sigma with the following manufacturer specifications: an average particle size of 31.55 μm, a Brunauer-Emmett-Teller (BET) surface area of 1100-1500 m^2 /g, and a bulk density of 0.4 g/cm^3. Hydrogen peroxide was 30% (wt.) from Sigma, and hydrochloric acid (HCl) was of an HPLC grade from Pharmco. 6-Thioguanine (6-TG) was of 98% purity from Sigma. Dimethyl sulfoxide (DMSO) was of an ACS grade from VWR, methyl tert-butyl ether (MTBE) of the ACS grade (98 %) was from EMD-Millipore, and n-dodecane (pure, ≥99 %) was obtained from Acros Organics. The materials to prepare buffer solution, namely sodium chloride, potassium chloride, and anhydrous sodium and disodium phosphate were of an ACS grade from Baker. The materials for preparation of the HPLC mobile phase were an HPLC grade methanol and glacial (99.7+%) acetic acid from Pharmco, an ACS grade sodium hydroxide pellets from VWR, and an ACS grade (97%) sodium acetate from EMD Millipore. The fluid in the temperature baths was ethylene glycol (97%) from Pharmco.

2.2 Activation of A100 and formation of hydrated A100

Due to free 1,4-benzenedicarboxylic acid remaining in the raw A100 material after synthesis, a regimen with heating and vacuum was developed to remove impurities and “activate” the MOF for further encapsulation[51]. However, due to hygroscopic nature

of the activated A100, the further procedures were developed to keep the sample isolated from ambient atmosphere until addition of the solution for encapsulation. First, a 7.5 mL brown borosilicate glass vial was cleaned with a mixture of hydrogen peroxide and hydrochloric acid. The vial was then filled with 1 or 2 mmol of A100 (approx. 200 or 400 mg) and placed in a Lindberg/Blue M vacuum oven. The sample is heated to 170 ºC and held under a vacuum of 500 mm Hg minimum (provided by a diaphragm pump, model GAST RAA-P103-EB) for at least 2 hours. Once this is completed, the oven chamber was slowly flooded with pre-purified argon or nitrogen gas and the vial with sample, when cool enough to manipulate, was closed with a polytetrafluoroethylene (PTFE) cap under argon, becoming the activated A100 (actA100). If the A100 was used for preparation of an encapsulation complex, it was then transferred to a glove bag/box under argon to begin the encapsulation process. However, if the sample was to be "hydrated" (by adsorption of water vapor from air), it was transferred to a hydration chamber. This chamber was a screw-top tightly closed jar fitted with an elevated surface surrounded with a minimum of 50 mL deionized (DI) water. The uncapped vial with actA100 was placed on the elevated surface, the jar was closed with a lid, sealed with Parafilm and allowed to stay for 24 hr. at ambient temperature. During this time, water vapor filled the sealed chamber and became available for adsorption by the activated A100. Following this step, the vial was removed, closed with its PTFE cap, sealed with Parafilm and stored in a refrigerator at 5 ºC for further analysis. The so prepared material is referred to as hydrated A100 (hyA100).

2.3 Preparation of complexes A100-DMSO and A100-DMSO-6TG

For every vial of actA100, 5 mL of fresh 0.2 M solution of 6-TG was prepared by mixing the drug in DMSO and sonicating (sonicator model Branson 1510). This 5 mL volume was pipetted to a vial of actA100 under argon in a glove box/bag and then removed from this box/bag. A 1 cm round magnetic stir bar was added to the vial, the vial capped with a pre-weighed aluminum foil and laced back on the vial, and the vial placed on a stirring hotplate to be stirred at 120 revolutions per minute (rpm) for 24 h. After this, the stir bar was removed, and the vial is spun in a centrifuge (Centrific Model 228) at 3,300 rpm until a suspension-free supernatant is clearly visible (typically between 30-45 minutes). This supernatant was collected by pipet and reserved for further analysis. As some unencapsulated 6-TG may still be on the surface of the obtained powder, the sample was then washed with an additional 2 mL of DMSO. The sample was then centrifuged for 15 min. and its supernatant added to the previous one. As the sample was to be dried in vacuum at ambient temperature (due to the possible heat degradation of 6-TG), any remaining unencapsulated DMSO (which has a relatively low vapor pressure) was washed away with MBTE (which has a higher vapor pressure). The sample was washed with 2 mL of MBTE, centrifuged for 15 min, and the supernatant collected and reserved. The, the process was repeated. To produce the complex A100-DMSO, the process was similar. However, instead of solution of 6-TG in DMSO, a 5 mL of DMSO was used for the adsorption step, and washing with DMSO after removing the first supernatant was omitted.

In both cases, after the final centrifuging and removal of the supernatant, the

encapsulated sample has been dried at room temperature in a vacuum of a single-stage rotary vane pump (model Zeny) with pumping speed of 3.5 cubic feet per minute (CFM) and base pressure 50 mTorr. The vacuum was applied until the constant mass is achieved (approx. 36-48 h). Vials with samples were then closed with caps, sealed with Parafilm and stored in a refrigerator at 5 ºC. Both A100-DMSO (the binary complex) and A100-DMSO-6TG (the ternary complex) were synthesized at least in triplicate.

2.4 Sample characterization

Gravimetric analysis was conducted using analytical balance Mettler AG-204. Differential scanning calorimetry (DSC) measurements were performed using the apparatus from TA Instruments (model 2920). The standard DSC scans were accomplished using the standard sample cell under purging with argon at a heating rate of 5 ºC/min. The modulated scans (MDSC) were performed using the refrigerated cooling system (RCS) cell under nitrogen purging at a heating rate of 2 ºC/min and a modulation rate ± 1 ºC in a 100 sec. period. Solid samples were prepared in aluminum non-hermetic pans, while liquid samples were in aluminum hermetic pans.

The X-Ray diffraction (XRD) patterns were collected from samples, which were manually ground in agate mortar and pestle, hand-pressed into the 1 mm deep flat quartz sample holders, and covered with a 10 μm thick polyethylene wrap to protect from adsorption of water vapor in ambient air. Samples were analyzed using Rigaku MiniFlex diffractometer at a Cu K-alpha line at 0.15418 nm at the 2θ increments of 0.02 degrees over the range of 2θ = 5 - 40 deg.

The encapsulation supernatant and solutions containing the released drug were analyzed using an HPLC instrument (Agilent 1100) following the modified protocol of detection of 6-TG. The reported protocol used acetate buffer with pH 3.5 (with 10 % methanol) as mobile phase[52]. It has been modified to be conducted using an isocratic pump and a LiChrospher 100 RP-8 (5 μm) column at 25 ºC and flow rate of 2 mL/min. Injection volume was 1 μL and the monitoring conducted at the wavelength of 345 nm. To calculate peak areas in the HPLC traces, numeric curve fitting was conducted using Microcal Origin 2015 program Student Edition, and its mathematical functions Gaussian and GaussMOD.

2.5 Sample characterization by solid-state conventional and synchronous fluorescence spectroscopy

Fluorescence spectra were taken using Fluorolog Tau-3 spectrometer (Horiba Scientific) which is equipped with dual monochromators, a T-arrangement sample compartment, and a xenon flash lamp as photoexcitation source. The spectrometer was connected to an automatic voltage regulator (Norstar DAVR-3000 PRO) to minimize variations in the lamp output due to fluctuations in the incoming grid voltage. Further fluctuations of the signal detected at the sample detector (S) were minimized by dividing this signal by the voltage obtained at a reference detector (R) installed before the sample chamber. This ratio (S/R) compensates for changes in the detector response due to changes in the brightness of the incoming light (which reaches both the S and R detectors), while not affecting the signal due to the light interacting with the sample (only

observed by the S detector). Solid samples were contained in 700 μL quartz cells capped with the PTFE stoppers and sealed with Parafilm. Solid samples were contained in the dual-position thermostat cell holder (model FL-1012), and studied either at room temperature or when heated by a water/ethylene glycol mixture passing through the FL-1012 cell holder.

The "conventional" solid-state fluorescence emission spectra were recorded with the photoexcitation wavelength λ_{ex} constant within each spectrum, while the photoemission wavelength λ_{em} was swept within 230-500 nm at a step of 0.5 nm, with optical slit set at 3 nm. Then, the λ_{ex} was changed at the 10 nm increment and another emission spectrum collected; overall, the λ_{ex} was changed from 240 nm to 500 nm. The "conventional" solid-state fluorescence excitation spectra were recorded with λ_{ex} varied within 250-520 nm at a step of 0.5 nm, while the λ_{em} was varied from 240 to 400 nm at the 10 nm increments, using optical slit at 3 nm.

For the solid-state synchronous fluorescence spectra, the λ_{em} and λ_{ex} were adjusted simultaneously in the range of 240-500 nm, and the increments were set as the difference between the λ_{em} and λ_{ex} ($\Delta\lambda = \lambda_{em} - \lambda_{ex}$). The $\Delta\lambda$ was varied at the 10 nm increments. For the high resolution synchronous scans, the $\Delta\lambda$ was varied at the 2 nm increments. The optical slit width for the high-resolution synchronous scans was 2 nm, and all experiments were conducted under the atmospheric pressure.

Numeric analysis of the fluorescence spectra was performed with Microcal Origin 2015 program Student Edition.

2.6 Release of 6-TG from A100-DMSO-6TG complex in the form of powder

A phosphate buffer saline (PBS) was prepared at pH 7.4 and kept at 5^{o}C until used, to discourage bacterial growth. The temperature bath with stirring was created by connecting an oil bath (Ace Instatherm) to an Auber fuzzy logic proportional integral derivative (PID) controller. The PID controller detected bath temperature via a K-type thermocouple. A 100 mg of sample was hand ground fine in an agate pestle and reserved. A 100 mL of PBS was held at 37 ^{o}C in a 150 mL beaker inside the above bath. This solution was stirred at 60 rpm, and the 100 mg of ground sample was added to it (corresponding to a zero time of drug release) At the given sampling intervals, a 1 mL sample was removed via a disposable syringe. A 0.2 μm filter tip was then attached to the syringe, and the sample pushed back through it to collect the clear filtrate into an HPLC vial for further analysis. After each sampling, the drug release suspension was returned to its initial volume by adding 1.0 mL of PBS. The sample vials were collected and refrigerated at 5 ^{o}C until such a time that they could be analyzed together by HPLC-UV. The reference specimens were prepared similarly, except that 1.0 mL of an 8.3 mM solution of 6-TG in DMSO was added to the PBS instead of a powder sample.

2.7 Release of 6-TG from A100-DMSO-6TG complex in the form of pressed pellet

The same temperature bath and PBS solution as above was used for drug release from the sample in the form of a pressed pellet. A 50 mg of sample was hand ground fine in an agate pestle and reserved. The smaller tungsten carbide rod (lower punch), see Figure 5, was loaded into the cylinder with small central through hole (anvil) in such a way that the smooth side of the lower punch faced up. This lower punch and anvil were then set inside the black-rimmed base with vacuum nozzle.

Figure 5a. Photo of pellet die, disassembled

Figure 5b. Photo of pellet die, partially assembled

The previously prepared powder sample was then poured in the central through hole of the anvil, on top of the lower punch. The long tungsten carbide rod (the upper punch) was then set in the through hole in the anvil, smooth side down, compressing the sample under light hand pressure. The assembled pellet die, seen as in Figure 6, was then inserted in a hydraulic Carver press.

Figure 6. Photo of pellet die, assembled

The valve on the press was turned clockwise until its stop, and pressure lightly applied on the pellet punch until it was seated firmly in place. A vacuum line (a GAST diaphragm pump, model DOL-101-AA) was connected to the nozzle on the base and vacuum applied for two minutes. The hydraulic pressure was then steadily increased up to 6.5 tons and held at that pressure for 2 minutes under vacuum. The vacuum tube was disconnected, and then hydraulic pressure released. The entire pellet die assembly was then removed from the hydraulic press, and the anvil (still containing the bottom and top punch) was removed from the base. The top punch was placed over a shallow metal release ring and struck with a rubber mallet once or twice to loosen the bottom punch enough to remove it by hand. Having done so, the top punch was carefully malleted until such a point where the pelletized sample could be exposed and removed with tweezers

A release vial for the pellet was prepared from a 1 cm^2 piece of a stainless steel mesh #500, a series of 1.0 mL conical interior micro vials with 13 mm open-top caps and 12 mm rubber/PTFE septa, and Spinvane triangular stir-bars for micro vials, Figure 7.

Figure 7. Photo of pellet release vial, disassembled

The stir-bar was inserted and the square of stainless steel mesh was fitted, using the upper punch from the die press, into the opening of the conical vial to form a 6.5 mm circular cage. The vial was then filled with approx. 1.2 mL of PBS (the volume needed to cover the top of pellet) and the pellet inserted into the mesh cage.

Figure 8. Photo of pellet release vial, assembled

The vial was covered with a PTFE cap and heated in the bath at 37° C with the stirrer rotating at 60 rpm. At the given sampling intervals, the cage containing the pellet was transferred to a vial containing fresh PBS solution and a stir-bar, and the previous vial was sealed and refrigerated at 5° C until such a time as the samples could be analyzed together by HPLC-UV.

3 Results and Discussion

3.1 Characterization

3.1.1 Drug 6-TG in HPLC

The external standards of 6-TG in DMSO (diluted with 7.4 PBS) produced a single peak centered at the retention time (RT) of 2.76 min. with a consistent tailing expressed across all samples when analyzed at 345 nm. A calibration curve (Figure 9) was constructed over the range of drug concentration 0.05 mM to 0.2 M with an R^2 value of 0.97.

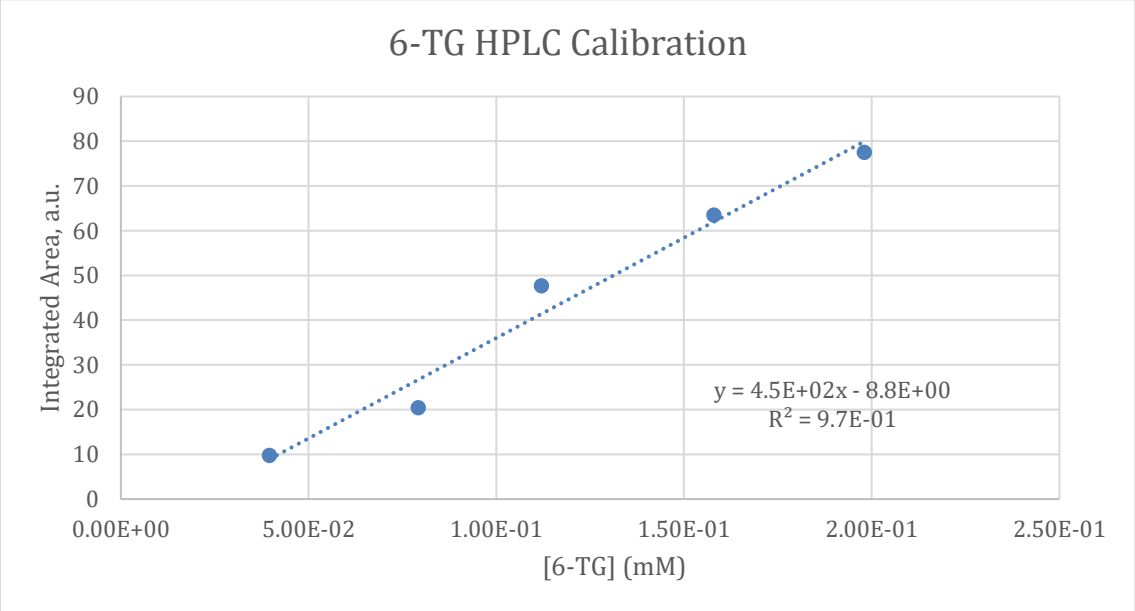

Figure 9. The HPLC-UV calibration curve of 6-TG at 345 nm

3.1.2 Gravimetric analysis of binary and ternary complexes

The post-activation A100 is expected to show a ≈10% decrease in mass due to evaporation of precursors of organic linkers in raw material[51]. The initial samples showed this decrease almost exactly, while the later prepared samples showed a higher mass decrease associated with a higher level of impurity in the raw material due to a new container of material being used. The 6-TG amount present in the sample, as determined from the difference of the HPLC-UV analysis of the supernatant before and after encapsulation, was subtracted from the overall mass to determine the amount of co-encapsulated DMSO. In addition, samples without 6-TG (binary complex) were created and analyzed gravimetrically.

Complexes with the two types of stoichiometry were produced. Basolite A100 which adsorbed DMSO had the nominal stoichiometry of $[A100]_x[DMSO]_y$ and such samples were referred to as the "binary complexes". Samples which adsorbed both DMSO and 6-TG had the nominal stoichiometry of $[A100]_x[DMSO]_y[6\text{-}TG]_z$ and were referred to as the "ternary complexes". The stoichiometry of the binary complex was found to be $[A100]_2[DMSO]_3$ and that of the ternary complex was found to be $[A100]_2[DMSO]_3[6\text{-}TG]_1$. The relative non-stoichiometry of the ternary complex compared to the binary complex is notable, as it suggests a more complicated bonding structure than 1 guest molecule per pore. In addition, the differences in the stoichiometry between the binary and ternary complexes suggest that the 6-TG is not simply displacing a DMSO molecule already encapsulated in the complex. Finally, results of the hydrated

A100 (Hy-A100) prepared in the hydration chamber showed the expected 4 moles of water per mole of A100[53].

3.1.3 Conventional DSC analysis of A100 and complexes with guest molecules

The conventional DSC analysis of Hy-A100 (model compound), A100-DMSO and A100-DMSO-6TG show a common endothermic peak at 555 °C (as seen in Figure 10), which we can associate with thermal decomposition of A100 as in the literature [43].

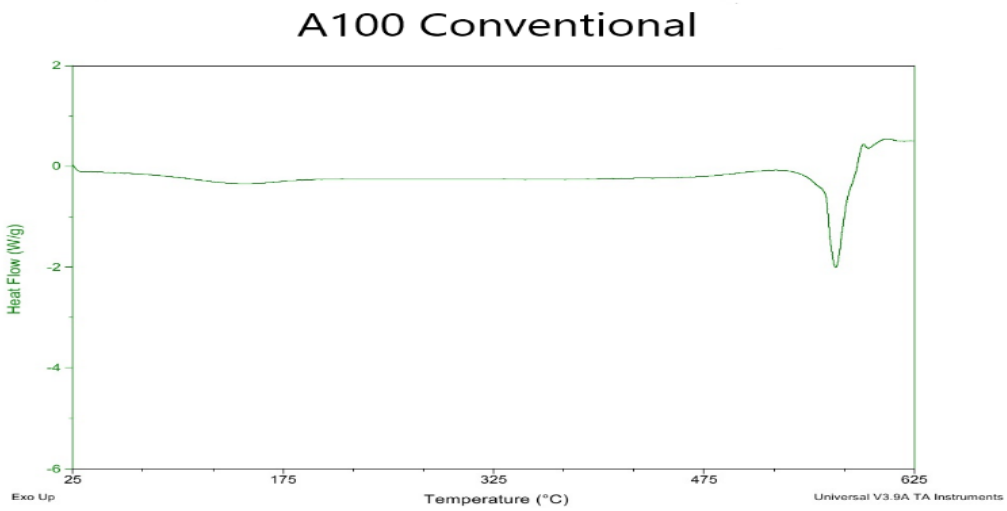

Figure 10. Conventional heat flow of Basolite A100

In Figure 11, there are several single peaks clustered in the 80-100 °C range which we associate with desorption of molecules. The water adsorption complex Hy-A100 has a deep, broad peak centered 100° C, the highest value in this range. This peak at 100° C is consistent with desorption of water. The binary complex A100-DMSO shows a shallower peak centered around 78 °C, while the peak of the ternary complex A100-DMSO-TG is

similarly shaped, but shifted to around 89 ˚C. A standard DSC scan of the activated A100 seen in Figure 10 did show a small amount of endothermic process observed as a peak also around 100 ˚C. However, the lab had no atmospheric chamber capable of holding the pan-crimping device necessary for hermetic specimen preparation. So, it is likely that this is related to water absorption from the atmosphere by the extremely hygroscopic activated A100. Nevertheless, this peak is consistent with the desorption temperature of water.

The comparison of the DSC peaks of the binary complex A100-DMSO to those of the ternary complex A100-DMSO-6TG shows an increase in desorption temperature, as seen in Figure 11.

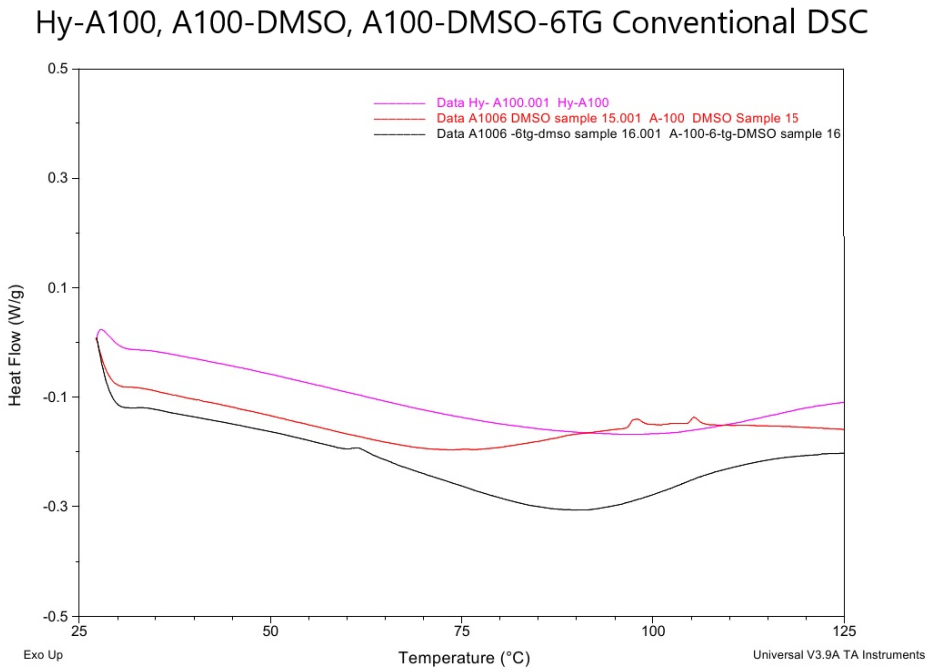

Figure 11. Conventional comparative DSC of Hy-A100, A100-DMSO, and A100-DMSO-6TG

As both complexes contain DMSO, it is expected that peaks <100° C are due to the desorption of DMSO. This was unexpected, as usually the presence of additional molecules in solution lowers the desorption temperature of the target adsorbate rather than increases it[54]. However, if the molecules of 6-TG were bound to organic linkers in the A100 while also still being bound to the co-adsorbed DMSO molecules, this could explain the higher desorption temperature for the ternary complex. In the other words, a DMSO molecule bound both directly to the A100 and to the co-adsorbed 6-TG, such as that in the ternary complex, would require a higher energy of desorption than a DMSO molecule only bound to the A100, such as that in the binary complex. The modulated DSC scans (MDSC) were performed to investigate this further and to help extract more detailed data from the broad peaks in the standard DSC.

3.1.4 Modulated DSC analysis of A100 and hydrated complexes

The data by modulated DSC (Figure 12) show the additional detail of the thermally induced desorption, with more endothermic peaks observed for the model complex Hy-A100. One peak was at the previously recorded temperature of 100 °C, while a new peak is observed at 80 °C. The peak at 100 °C has a corresponding peak at the same temperature in the reversible heat flow (solid lines) and a plateau in the non-reversible heat flow (dashed lines). The 80 °C peak had a corresponding peak at the same temperature in the non-reversible heat flow with no activity at that temperature in the reversible heat flow. The removal of adsorbed water at this point under strong purge conditions (like the ones the MDSC analysis was performed at) should show an irreversible process[49]. The adsorbed solvent (water) is desorbed, evaporates and is carried

away by the purge gas. This would suggest that the reversible heat process recorded at 100° C is not entirely due to loss of water (although the plateau of the non-reversible heat flow would suggest that some loss is still occurring here). An reversible effect that could occur in the MOF would be the breathing effect, as changes in the pore size occur [43].

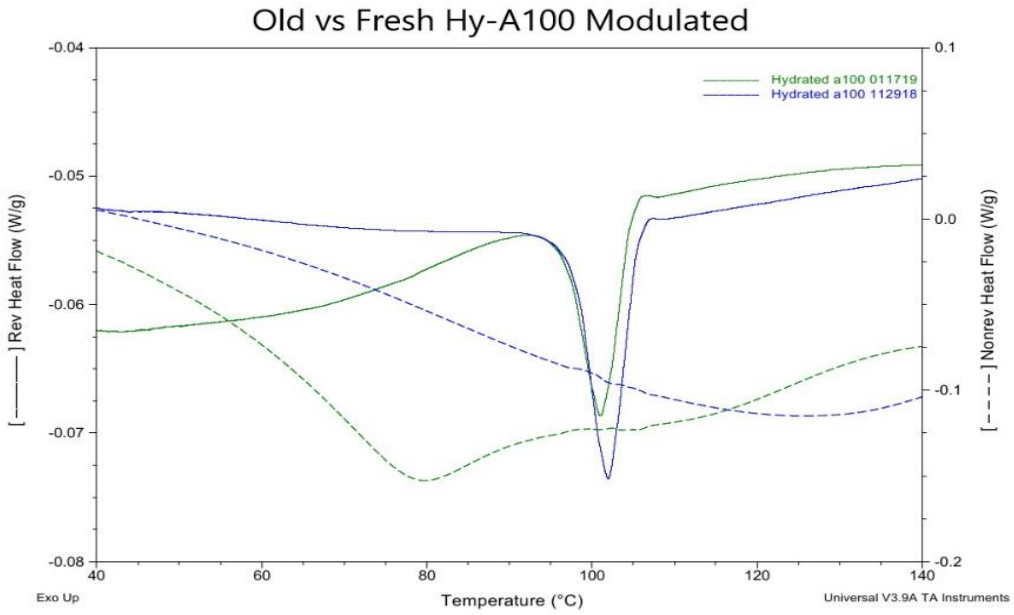

Figure 12. MDSC analysis of weakly and strongly hydrated A100

Additional support for breathing phenomenon was obtained, when a hydrated sample prepared few months earlier ("older sample") was analyzed by MDSC. The MDSC curve of the "older sample" is shown in blue color in Figure 12. While the activated A100 absorbs 4 water molecules when in an isolated hydration chamber, it has been shown to absorb 50-25 % of that amount under other conditions[51]. The older hydrated sample was determined to contain 2 moles of water per mole of A100. Given enough time, such as few months, this older hydrated sample had while being stored, it is

likely that it would return some of its excess water to the less hydrated ambient air. This is seen in the MDSC results of this sample, with the non-reversible heat endothermic peak missing from 80 °C as compared to the freshly hydrated sample. The "older" hydrated sample (blue curve in Figure 12) did still have the reversible peak and non-reversible plateau. This analysis suggests that A100 holds the adsorbed guest water molecules in at least two locations. The loss of guest molecules in one location can occur at lower temperatures and is not associated with any change in reversible heat flow, while the loss in the other corresponds with higher temperatures and a notable change in reversible heat flow is observed. We believe that molecules of one type are located inside the MOF pore and bound to organic linkers in some fashion, and the removal of them triggers the breathing effect. The other adsorbed water molecules must be located on a different location in the MOF and their removal does not reversibly alter the heat capacity of the A100 MOF.

3.1.5 Modulated DSC analysis of binary and ternary complexes

A reversible endothermic peak is seen also in A100-DMSO and A100-DMSO-6TG at 100 °C in Figure 13. Based on the previous Hy-A100 data (Figure 12), it is suggested that this peak is associated with a "breathing" effect. As DMSO is itself hygroscopic, it is likely that this peak describes an effect that is also seen in the hydrated sample.

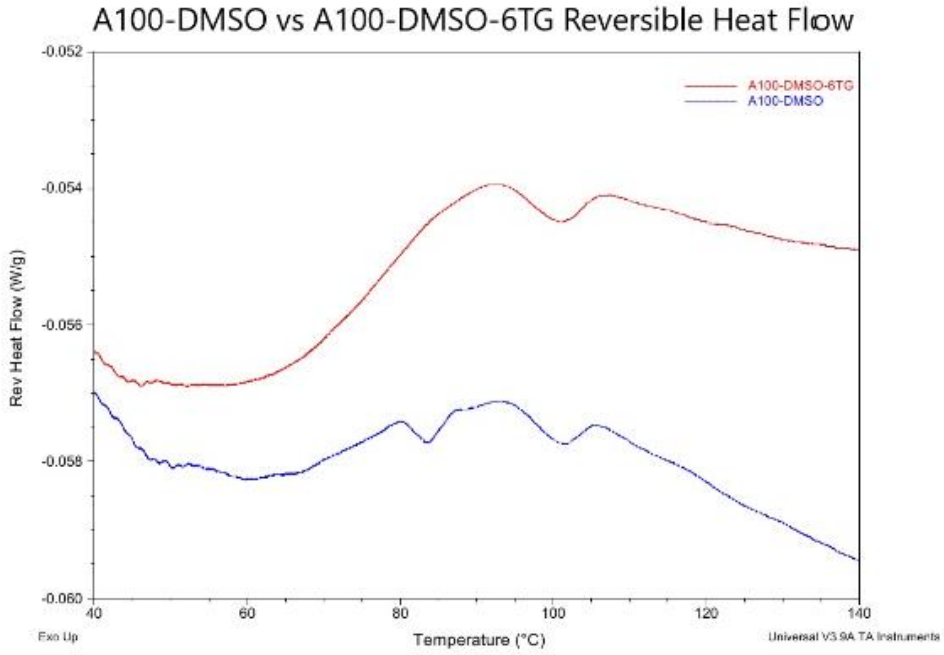

Figure 13. Reversible heat flow for A100-DMSO and A100-DMSO-6TG

In addition, there is a reversible heat flow peak at 85 °C in the A100-DMSO complex that is absent in the MDSC of the ternary complex. Its existence supports the data obtained in the standard DSC analysis, where there is DMSO available to adsorb/desorb in the binary complex that is absent in the ternary complex. The DMSO in the ternary complex is bound to the 6-TG in some way that inhibits this adsorption/desorption activity. The reversible heat flow at 85 °C is likely not related to any additional "breathing" in the A100-DMSO. While some MOFs do display multiple "breathing" states[55], Basolite A100 only displays two[38]. Additionally, as DMSO has a much lower vapor pressure than water, it is unlikely this peak is due to the evaporation of DMSO.

3.1.6 The room temperature XRD analysis of A100 and its hydrated complexes

The major XRD peaks of the activated A100 at room temperature (Figure 14) are consistent with the literature values for MIL-53(AL) see e.g. in Ref.[56] with the 2θ maxima found at 9, 12, 17.5, 21 and 26 degrees.

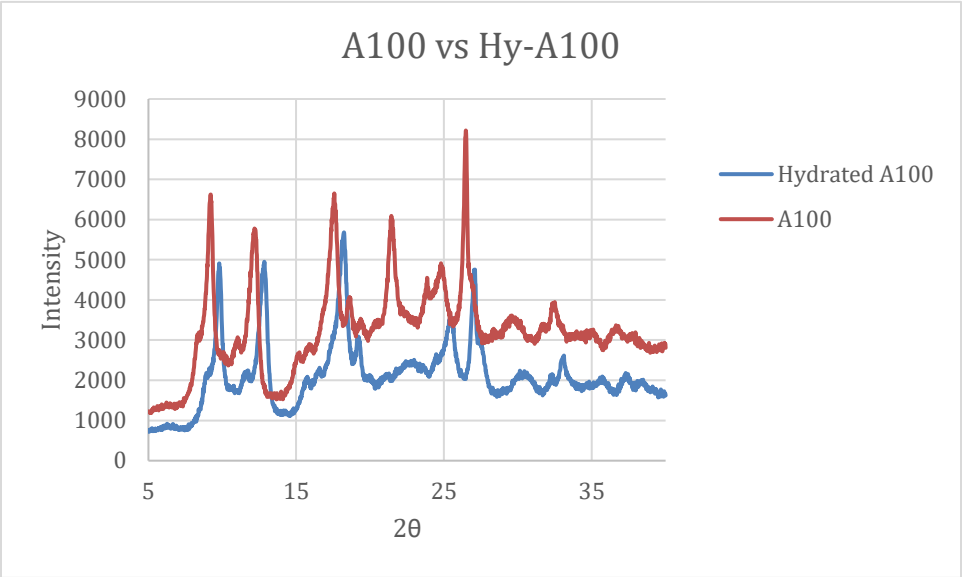

Figure 14. Activated MOF and Hy-A100 X-ray diffractogram

Upon hydration, most peaks experience a 1 degree shift to the higher values of 2θ, except the 2θ peak at 21 degree which has been eliminated. This is indicative of a hydration related "breathing" effect which reversibly alters the pore size of the MOF and thus changes its crystal structure and the diffraction pattern[57].

3.1.7 XRD analysis of Hy-A100 under variable temperature

Figure 15 can be used to compare Hy-A100 that was heated to 100 ˚C to both the unheated Hy-A100 and the original A100. In that comparison, the XRD pattern largely matches that of the A100.

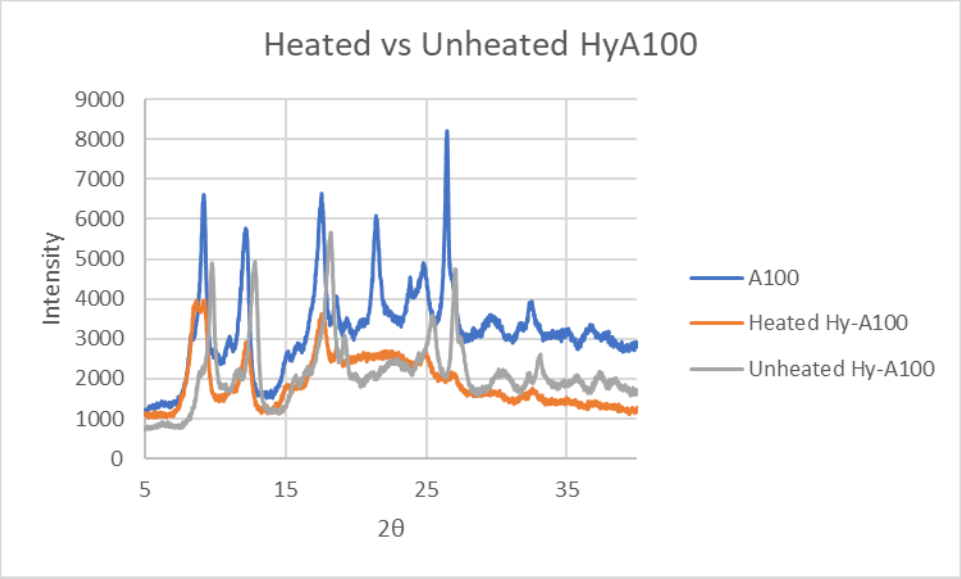

Figure 15. X-ray diffractograms of heated and unheated HyA100 with A100 reference

This is in accordance with the idea that, once the guest molecules have been removed from the MOF, the “narrow pore” structure undertakes “breathing” and returns to its “wide pore” configuration. A few notable differences remain though. First, the double peak at 2θ = 9 degrees is now smaller in the heated Hy-A100, whereas in the unheated Hy-A100 the right shoulder was substantially higher. Testing showed this shoulder being very sensitive to hydration under ambient atmospheric conditions. It has increased over the subsequent XRD scans of the same (dried) sample, when it was adsorbing water from air inside the sample chamber. However, the signal at 2θ =21

degrees was still suppressed as it was in the fully hydrated sample. This suggests that either that the recovery to the original pore configuration was not complete, or that some degradation occurred to the MOF being held that this temperature over the long course of the analysis (several hours). Lastly, the peaks at 2θ > 21 degree are drastically reduced compared to the activated A100. This may be related to some heat-related degradation or partial loss of adsorbed water.

3.1.8 XRD analysis of binary and ternary complexes

Similarly to the room temperature XRD patterns of water encapsulated on to the activated A100, encapsulation of DMSO and DMSO-6TG on the activated A100 resulted in a change in the crystal pattern of the A100. As seen in Figure 16, the 2θ peak at 9 degrees for the A100 appears to have been shifted by one degree, with this being similar to one or two-degree shift occurring at the 17.5, 21 and 26 deg. peaks. The peak at 2θ = 12 degree in A100 seems to have been suppressed, and a new peak in A100-DMSO occurs at 2θ = 16 deg. These findings are all indicative of shrinking of the 3D lattice of A100 (as DMSO molecules should not be observed in the X-ray analysis) and likely show an overall change in symmetry of the lattice. A known crystal structure to fit this pattern by the standard Rietveld refinement has not yet been found.

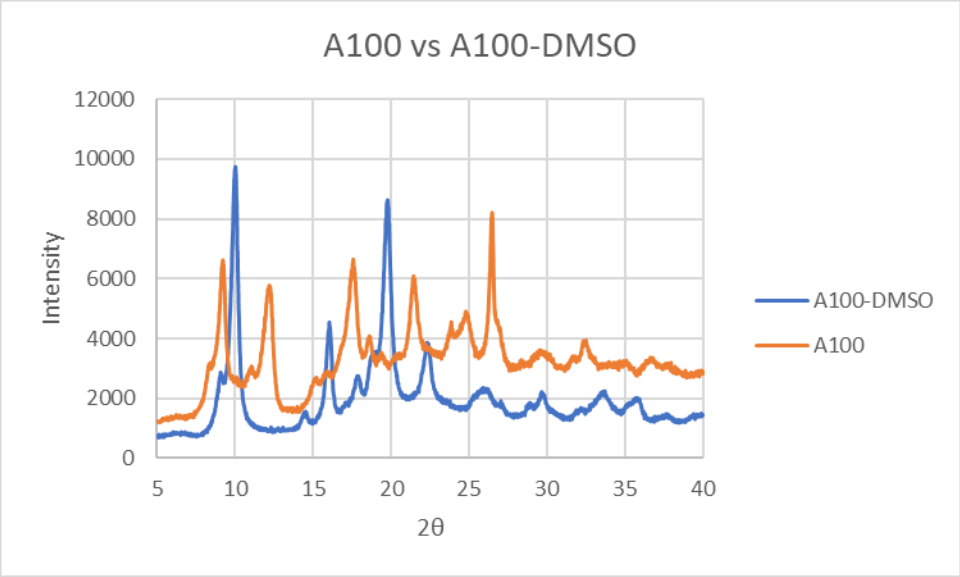

Figure 16. A100-DMSO vs A100 X-ray diffractogram

It is also notable that the diffraction pattern of A100-DMSO does not shift in relation to A100 as that of Hy-A100 did. When A100 became hydrated to form Hy-A100, the peaks of its XRD pattern shifted by a uniform amount of ca. 1 degree to the higher angles, with some peaks becoming drastically reduced in intensity. Interestingly, when A100 adsorbed DMSO to become the binary complex, the shift did not occur in the same way. Notably, the addition of water to A100 has suppressed the signal at 2θ =21 deg. while DMSO has suppressed the peak at 2θ =21 deg. Additionally, the 2θ peak at 17.5 degrees appears to have shifted to the lower, rather than higher 2θ. This suggests that the DMSO and water may be bound differently inside the A100 pore.

The modulated DSC analysis of A100-DMSO suggested that while an endothermic peak occurred around 75 °C, this is related to a non-reversible process. This peak was thought to be correlated to the desorption of the non-linker bound DMSO and should not have been accompanied by any “breathing” effect in the A100. Because of

this, the material at 75 °C should be free of the pore changes that would be detectable as a different crystalline form. As the XRD patterns of A100-DMSO at room temperature and at 75° C show (Figure 17), no significant changes in the overall pattern occurred.

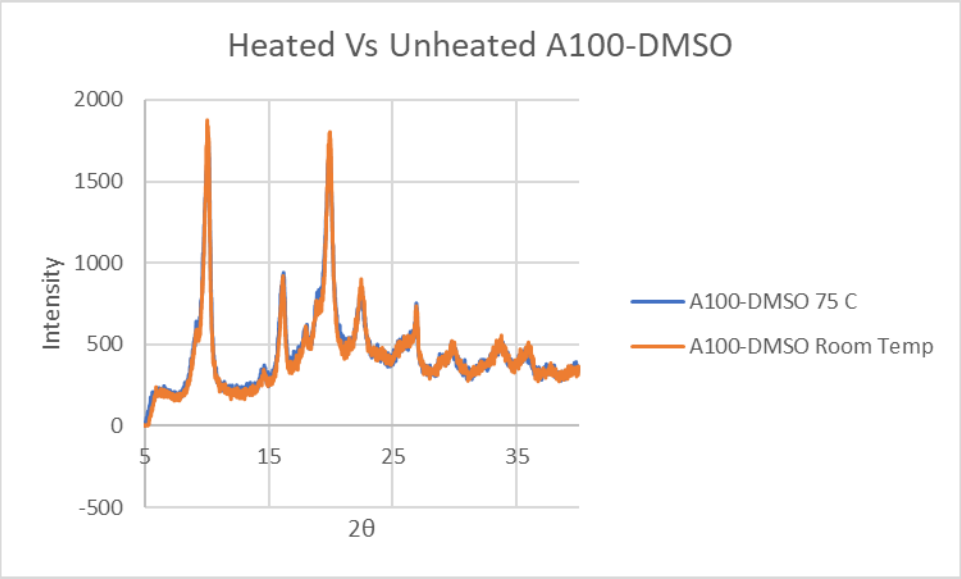

Figure 17. Temperature dependence of A100-DMSO X-ray diffractogram

A comparison between the XRD patterns of the binary and ternary complexes (Figure 18) shows a great deal of agreement. All major peaks in the pattern of the A100-DMSO appear at the same values of 2θ as those of the A100-DMSO-6TG. This would suggest that if the 6-TG molecule is bound to organic linker as suggested in the DSC analysis, its presence there does not change the crystal structure in any greater extent than DMSO does. The process that occurs when A100 adsorbs DMSO, whether it is "breathing" effect or not, is not altered by the presence of 6-TG in the MOF. Since it possibly means that the 6-TG molecule is not bound to organic linker, the additional analysis was performed via the solid-state fluorescence spectroscopy.

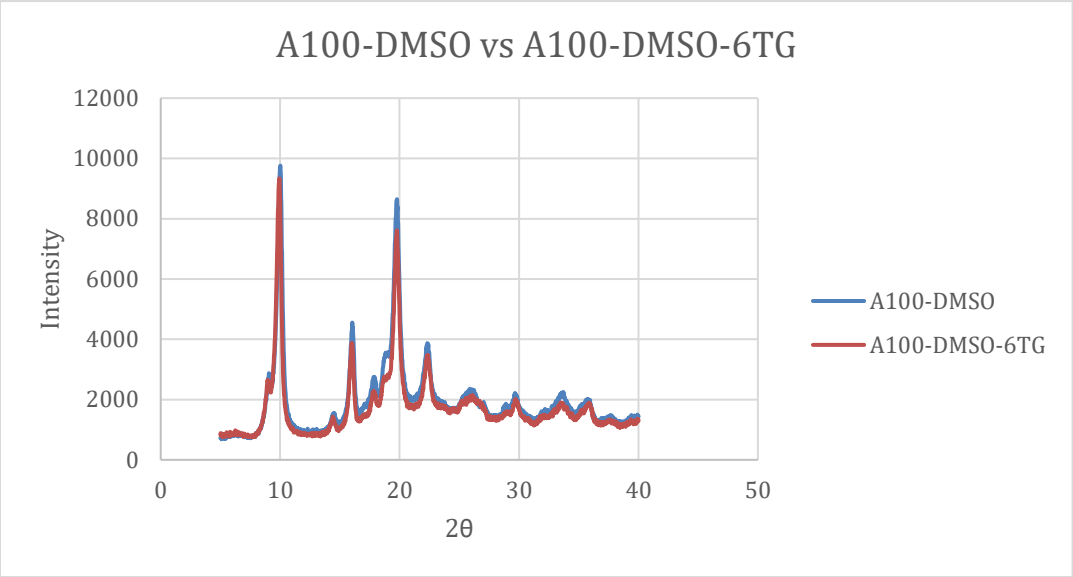

Figure 18. A100-DMSO vs A100-DMSO-6TG X-ray diffractogram

3.2 Fluorescence characterization

3.2.1 Conventional fluorescence emission spectroscopy of the sample vial

The conventional fluorescence emission spectra of the "background" were collected with the quartz cuvettes which hold samples. Such analysis was performed to verify that there was no significant contribution to the total fluorescence due to this "background". At λ_{ex} = 240-270 nm, the significant absorption by the quartz results in emission at about λ_{em}= 350 nm. Due to this detected artifact, all the subsequent measurements by "conventional" fluorescence spectroscopy began with λ_{ex} values no lower than 270 nm, Figure 19.

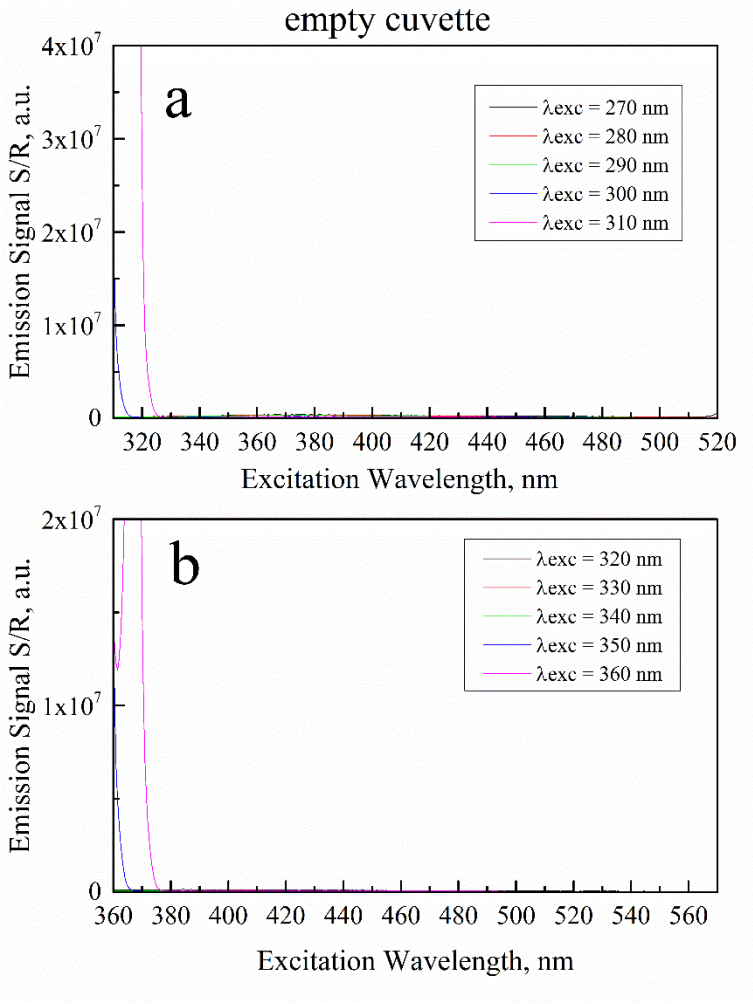

Figure 19a. Conventional excitation background spectra of cuvette, λ_{ex} 270-310 nm

Figure 19b. Conventional excitation background spectra of cuvette, λ_{ex} 320-360 nm

As seen in Figure 19, at $\lambda_{ex} \geq 270$ nm the contribution of emission from cuvettes to the overall fluorescence was minimal, and did not significantly contribute to the overall signal.

3.2.2 Conventional fluorescence emission spectroscopy of activated A100

The activated A100 shows two broad emission peaks (Figure 20a,b): 1) in the near-UV range at 390 nm and 2) in the visible range at 440 nm. For most spectra, the peak at 440 nm is of lower or the comparable intensity vs. the peak at 395 nm.

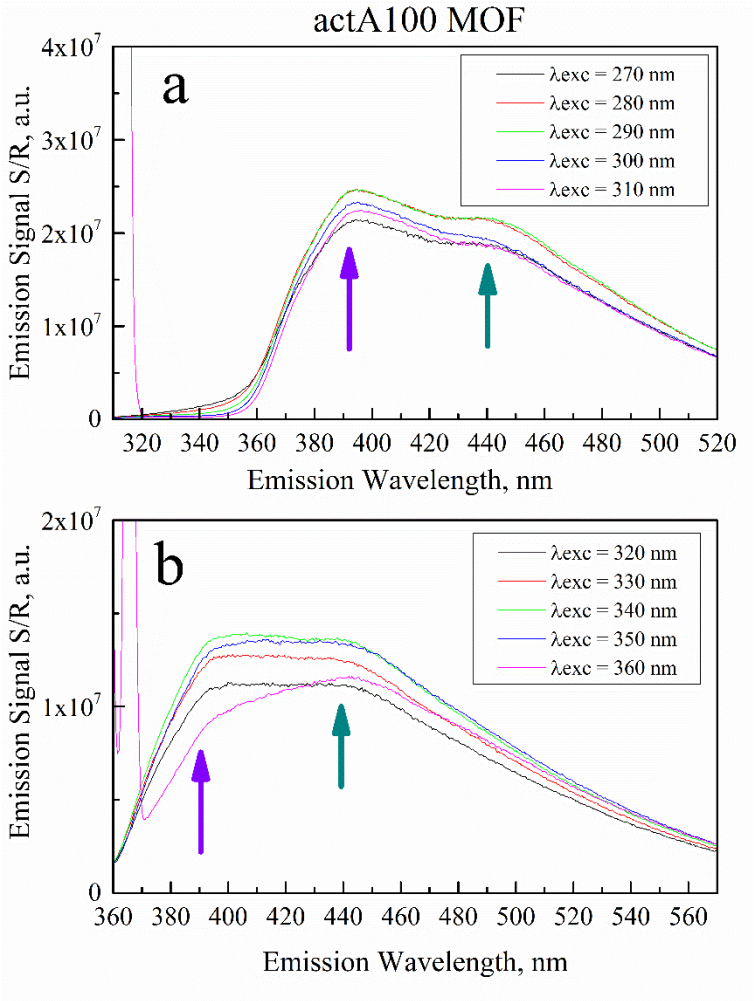

Figure 20a. Conventional fluorescence emission of activated A100, λ_{ex} 270-310 nm

Figure 20b. Conventional fluorescence emission of activated A100, λ_{ex} 320-360 nm

The peak at ca. 380 nm also corresponds, in part, to the fluorescence spectra of disodium terephthalate (Figure 21).

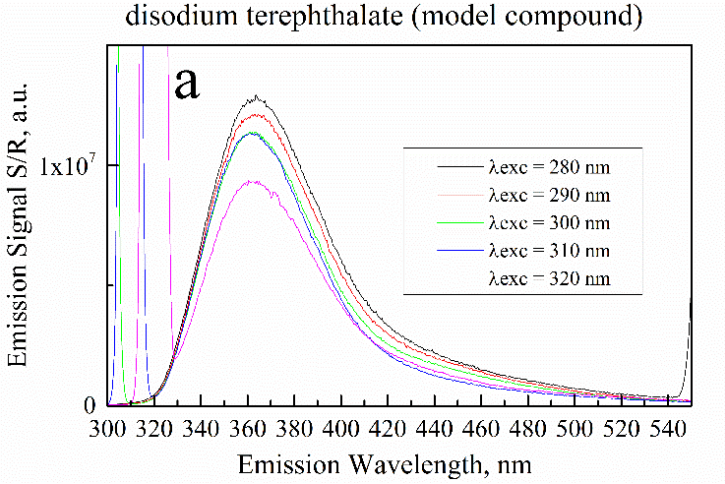

Figure 21. Conventional fluorescence emission spectra of disodium terephthalate

This model compound contains the dianion BDC^{2-} which is also present in organic linker of A100. Therefore, the emission in the "blue" range as in Figure 20 is due to the individual organic linker units in A100.

3.2.3 Conventional fluorescence emission spectroscopy of binary complex A100-DMSO

When comparing the "conventional" fluorescence spectra of A100 to A100-DMSO (Figure 22a), it's first important to note that the DMSO molecule absorbs light at around 215 nm as in Ref.[58], so it should not contribute to the spectra as the λ_{ex} for all materials was >260 nm. The spectra indicate that molecular orbitals (MOs) of the binary complex A100-DMSO are formed mostly by the MOs of A100. The spectra of A100-DMSO show an overall decrease in the signal intensity versus A100, which is associated with quenching by the non-fluorescent guest molecules of DMSO.

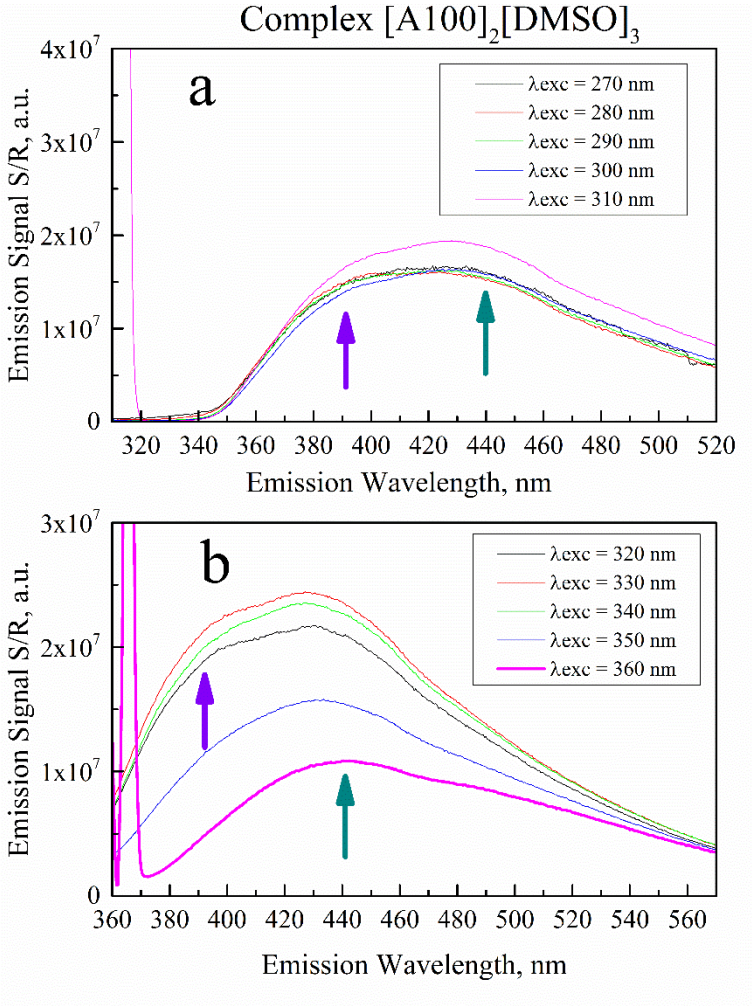

Figure 22a. Conventional fluorescence emission spectra of A100-DMSO, λ_{ex} 270-310 nm

Figure 22b. Conventional fluorescence emission spectra of A100-DMSO, λ_{ex} 320-360 nm

However, there was an area associated with the additional decreases in signal intensity. The peak at $\lambda_{ex} \geq 350$ nm was considerably lower for the binary complex A100-DMSO when compared to the activated A100. This indicates changes in the optically absorbing states in A100 after adsorption of DMSO. In the activated A100, the visible emission peak (around 440 nm) is almost always weaker, or at best of the same intensity as the near-UV peak (emission at ca. 390 nm), whereas in A100-DMSO this peak is

almost always stronger. This shows changes in the emissive states of A100 after adsorption of DMSO, and it results from electronic interactions in the complex. Recent studies on the solid-state "conventional" fluorescence emission spectra of naphthalene described these two peaks in terms of monomers (i.e. the individual molecules) relating to the UV emission, and "excimers" (molecular pairs) relating to visible emission [59]. Based on conventional fluorescence spectra of model compound sodium terephthalate (a structural equivalent of the BDC linker), the emission peak at 390 nm can be assigned to that of the individual fluorophores (namely the individual BDC linkers). This means that the peak at 440 nm must correspond to "excimers"; in this case, those are two BDC linkers in A100 which interact by the ligand-to-ligand charge transfer (LLCT) mechanism.

MOFs are solids with periodic lattice and as such they have often been considered semiconductors[60]. Each of these lattices can be associated with a known band gap. The band gap of MIL-53(Al) has been determined by the UV-Vis diffuse reflectance (DRS) spectroscopy [60] to be 3.56 eV, which corresponds a wavelength of about 348 nm. By comparison of Figure 21b and Figure 23b, one can see that the band gap of A100 has increased after adsorption of DMSO. Namely, the λ_{ex} = 350-360 nm (with photon energy being less than the band gap) corresponds to the sub band gap photoexcitation in the binary complex [42]. This suggests that adsorption of DMSO has altered the band gap in such a way so that to change the emission spectra. However, the exact values of the band gaps of either the activated A100 or the A100-DMSO cannot be determined due to very broad "conventional" spectra.

3.2.4 Comparison of conventional fluorescence spectra of binary and ternary complexes

At the shorter excitation wavelengths, the spectra of A100-DMSO and A100-DMSO-6TG appear to be nearly identical, Figure 23a.

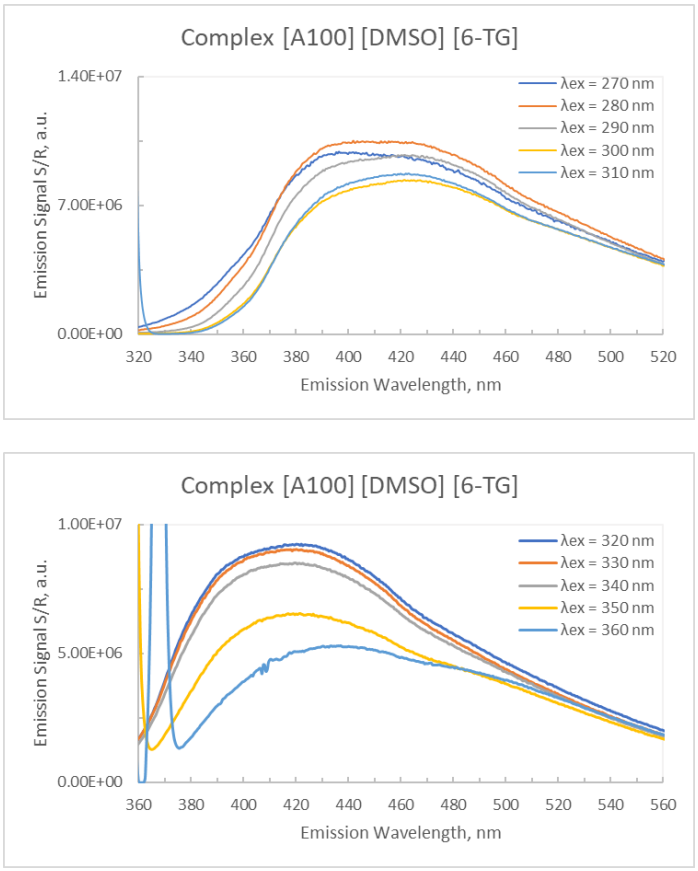

Figure 23a. Conventional fluorescence spectra of ternary complex, λ_{ex} 270-310 nm

Figure 23b. Conventional fluorescence spectra of ternary complex λ_{ex} 320-360 nm

The spectra in the visible range show a notable decrease in intensity across most of the emission range. This decrease did not change the position of the monomer (BDC linker) and excimer peaks. This quenching also diminishes as the λ_{ex} approaches the

absorption maximum of 6-TG at ca. 345 nm. When the peaks are analyzed relative to one another, a difference between the ternary and binary complex is seen. While the adsorption of DMSO quenched the peak associated with the "monomer" to such an extent that it was lower than the "excimer" peak, the adsorption of DMSO and 6-TG quenched this first peak only to the point where it was close to the "excimer" peak. In the UV excitation range, it does not appear that the 6-TG quenches the excitation of the "monomer" to the extent that DMSO does.

3.2.5 Solid-state synchronous fluorescence spectra of activated A100

To help establish a baseline material for further spectroscopic studies, A100 with no adsorbed guest molecules was analyzed first by solid-state synchronous fluorescence spectroscopy[61]. This analysis involved sweeping both the λ_{ex} and λ_{em} in concert with one another, with the difference between these two wavelengths ($\Delta\lambda$) being the variable set for each run.

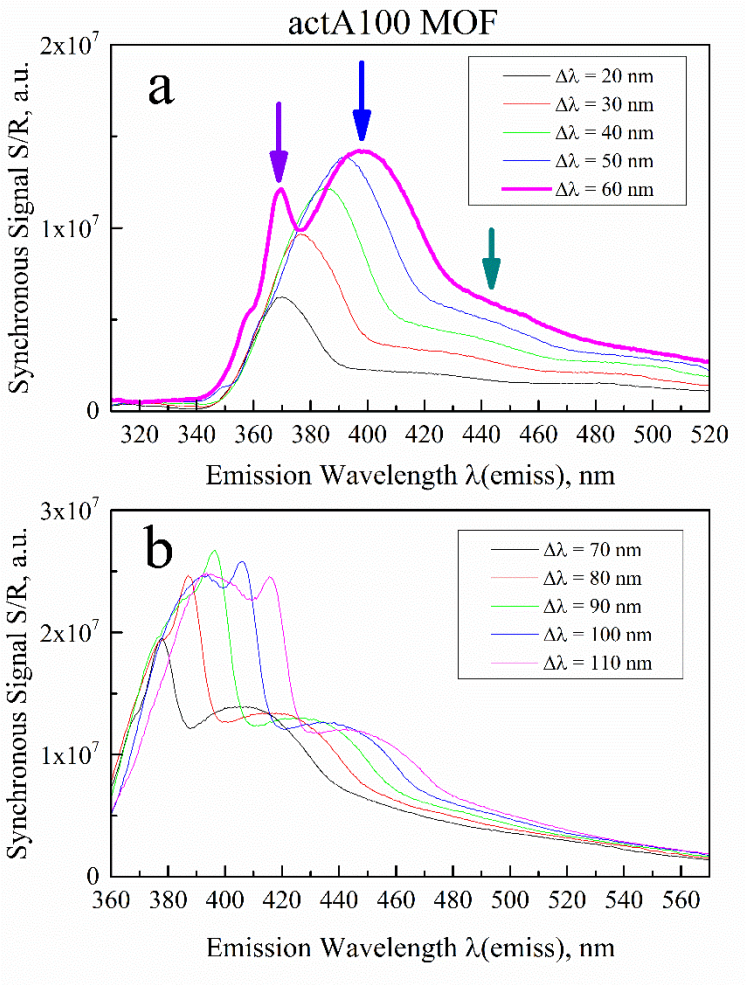

Figure 24a. Synchronous fluorescence spectra of A100, Δλ 20-60

Figure 24b. Synchronous fluorescence spectra of A100, Δλ 70-110

In the spectra of activated A100, the strong peak located at λ_{em} = 368 nm (Figure 24a) is due to absorption and the following fluorescence by the individual BDC linkers. This is supported by it located close to the absorption wavelength of the terephthalate anion in the diluted aqueous solution[53].

Also, the synchronous fluorescence spectra in the near-UV-visible emission range within 360-500 nm can be resolved into the individual peaks. Band gap calculations were

taken for $\Delta\lambda$= 60 nm, with its peaks analyzed by multi-Gaussian curve fitting. A full width at the half maximum (FWHM) was calculated for the shoulder (the monomer) at FWHM = 38 nm and for the peak (the band gap) at FWHM= 48 nm. This wider peak correlates to the band gap in activated A100. This band gap in flexible MOFs is formed by electronic interactions of least two organic linkers within at least one lattice unit. It is similar to, but distinct from, the "excimer" discussed earlier. The relationships between these three distinct electronic transitions are shown in Figure 25.

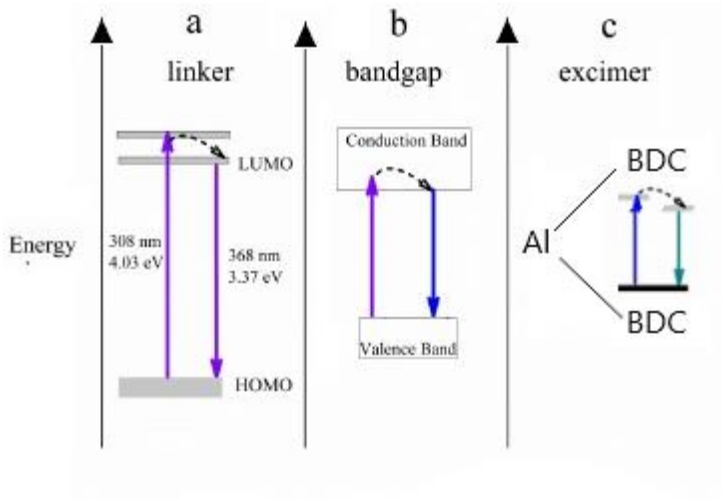

Figure 25. Scheme for electronic transitions in Al-MOF A100

To better reveal the additional information which the synchronous fluorescence spectroscopy can provide, the "conventional" excitation scans (where the λ_{em} was held constant while the λ_{ex} was swept across a range) were performed.

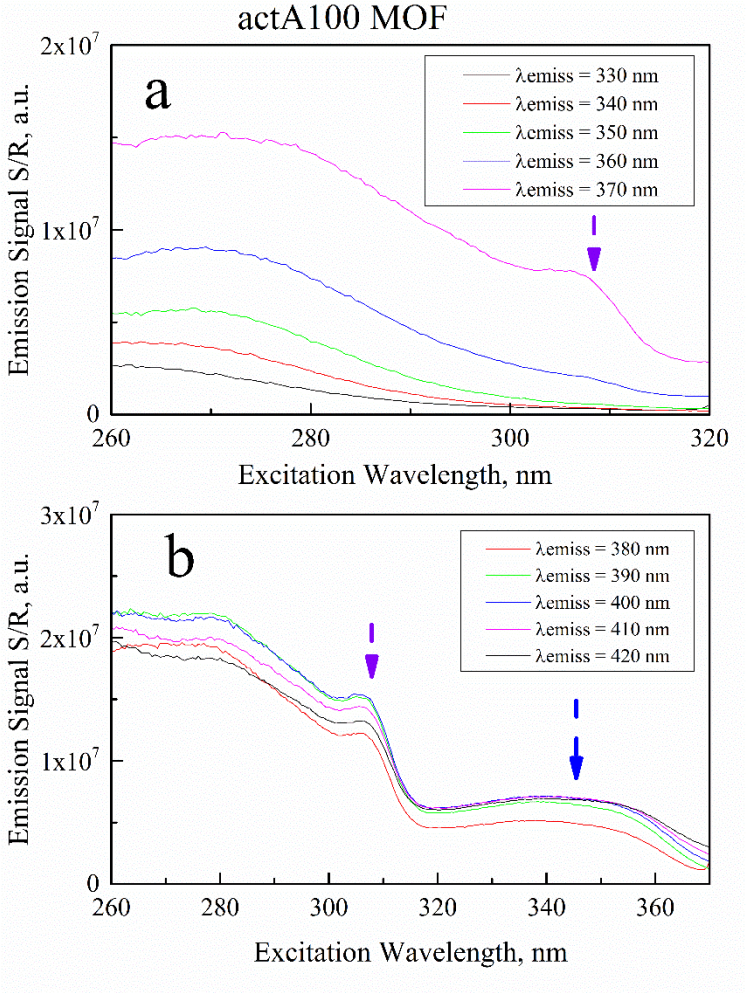

Figure 26a. Conventional fluorescence excitation spectra of A100, λ_{em} 330-370 nm

Figure 26b. Conventional fluorescence excitation spectra of A100, λ_{em} 380-420 nm

Spectra were collected in the range where the narrow resonance due to excitation of individual BDC linker was expected. In these spectra, the range of the λ_{ex} was limited to ≥260 nm due to limitations of the detector of the fluorescence spectrometer, and to ≤ 370 nm to avoid appearance of Rayleigh excitation artifacts (where λ_{ex} is close to λ_{em}). A weak shoulder at ca. 307 nm is observed. However, in the synchronous fluorescence spectra, the same transition is present as a well-defined, sharp peak which allows an

easier processing by numeric analysis. In addition, the anticipated band gap in A100 is observed through an elevated plateau at λ_{em} = 330-360 nm, compared to the distinct peak in the synchronous fluorescence spectra (Figure 26a).

3.2.6 Synchronous fluorescence spectroscopy of binary complex A100-DMSO

These synchronous fluorescence spectra can also help in the demonstration how electronic transitions revealed in the fluorescence of activated A100 are affected by adsorption of DMSO and the formation of complex A100-DMSO, Figure 27a,b.

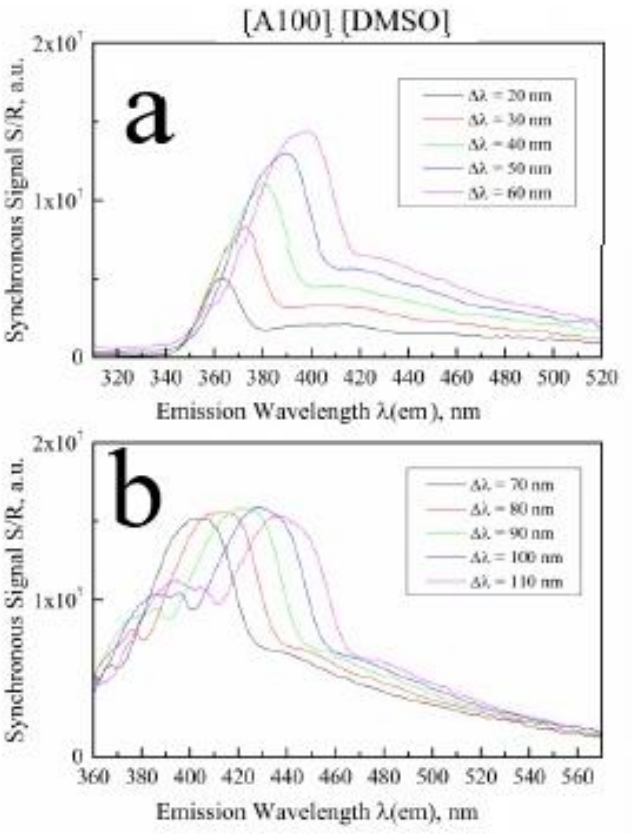

Figure 27a. Large Δλ synchronous fluorescence spectra of A100-DMSO, Δλ 20-60 nm.
Figure 27b. Large Δλ synchronous fluorescence spectra of A100-DMSO, Δλ 70-110 nm.

The sharp peak at λ_{em} = 368 nm, which was seen most strongly at Δλ = 60 nm, is absent. As this peak is associated with absorption of light by the monomeric individual BDC linker, its absence indicates electronic interactions of the individual BDC linkers with DMSO molecules in the binary complex. As the adsorption of DMSO is the only difference between the binary complex and the activated A100, the DMSO molecules must be bound directly to organic linker, to achieve this kind of strong effect.

3.2.7 Comparison of A100-DMSO and A100-DMSO-6TG complexes by synchronous fluorescence spectroscopy

Comparison between the spectra of the binary complex A100-DMSO and ternary complex A100-DMSO-6TG (Figure 28a,b) shows many similarities. The ternary complex still shows the blue-shifted maximum around 340 nm, which is associated with the band gap and the quenched peak of the "monomer" (in comparison with that of the activated A100) at 308 nm.

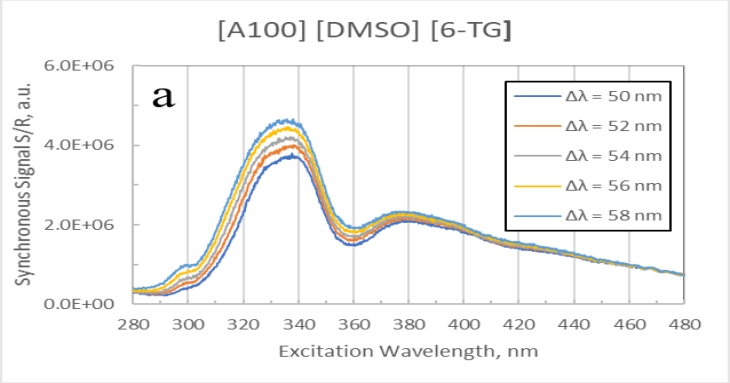

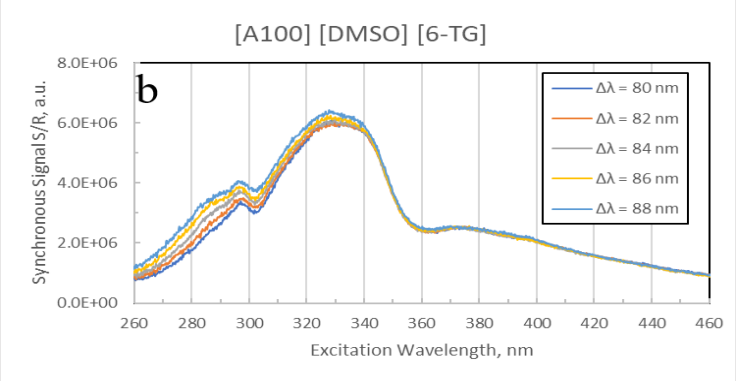

Figure 28a. Small Δλ synchronous fluorescence spectra of A100-DMSO-6-TG, Δλ 50-58 nm

Figure 28b. Small Δλ synchronous fluorescence spectra of A100-DMSO-6-TG, Δλ 80-88 nm

However, a subtle difference remains. While the “monomer” peaks of each complex have been quenched, the one of the ternary complex was quenched less, when compared to its main peak, than that of the binary complex. This is expected, as the π-π stacking can result in the enhancement of fluorescence and should not quench as much as the sulfur atom in the DMSO molecule. Additionally, the peak corresponding to the excimer around λ_{ex} = 380 nm is much higher compared to that of the binary DMSO complex. The presence of the hetero-aromatic 6-TG molecule does not inhibit the formation of the LLCT to the same degree as an adsorbed DMSO molecule does. Taking the data by the fluorescence spectra, together with the previous materials characterization, several conclusions can be drawn. The 6-TG molecule is bound to the linker and takes the place of DMSO in doing so. Additionally, the presence of the 6-TG molecule does not appear to trigger any additional band gap change or “breathing” effect as the peak associated with the band gap does not shift any further in the spectrum of the ternary complex, than it did in the spectrum of the binary complex.

3.2.8 Position of guest molecules in the binary and ternary complexes

At least two different sites are possible for encapsulation of guest molecules on to the A100: those bound directly to organic linker, and those bound elsewhere. As bonding to the linker is associated with a breathing effect, and thus a change in the electronic properties of the MOF, it can be most clearly seen using fluorescence spectra. Using solid-state synchronous fluorescence spectroscopy, we see that the addition of DMSO enables a blue shift of the band gap. This is indicative of bonding to the linker, and a possibly a change in the pore size.

When 6-TG molecule is added to the complex, quenching of the linker-associated "monomer" peak is reduced, while the peak due to band gap is unaffected. As the aromatic groups in the 6-TG molecule affect the fluorescence of groups in the BDC linker via the π-π stacking, the molecule of 6-TG must bind to this site, replacing the DMSO molecule. This is the effect which does not seem to noticeably induce an additional breathing.

The XRD data support this conclusion, showing that addition of any guest molecule (water, DMSO or 6-TG) triggers change in the crystal structure. However, while DMSO and 6-TG molecules show the similar shifts in the XRD patterns, they differ by the two peaks from those induced by water adsorption. This would suggest that while DMSO and 6-TG molecules have the similar affinity toward adsorption sites, water is different from them, since it induces different changes in the crystal structure. There are free hydroxide groups in the aluminum site in A100 which are not connected to organic linker; the bonding scheme is in Figure 29.

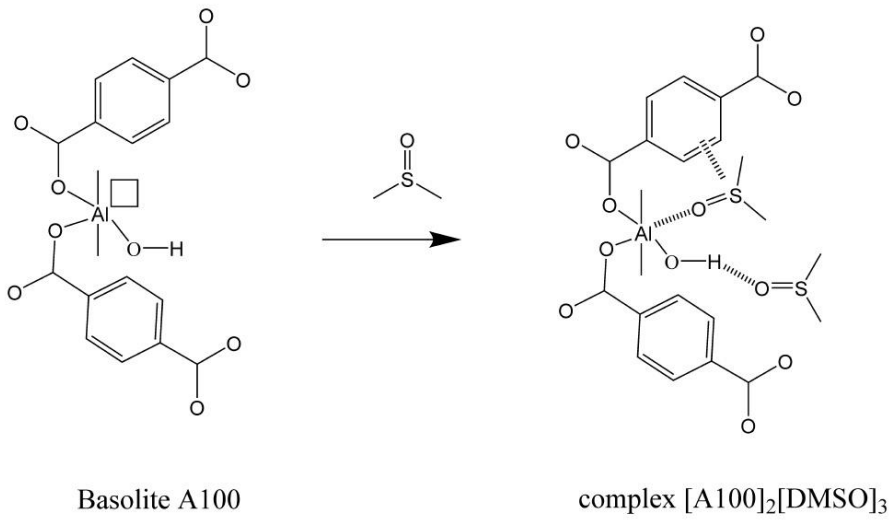

Figure 29. Bonding scheme for A100-DMSO

For any unit cell of A100-DMSO there are, on average, 1.5 DMSO molecules. One DMSO molecule is bound to the BDC linker, and the other one is shared between the two units. This would account for the stoichiometry $[A100]_1[DMSO]_{1.5}$ or, when rounded to integers, $[A100]_2[DMSO]_3$.

It's also important to note that while there is some evidence that the 6-TG molecule is bound to both the linker and the -OH group, the stoichiometry of the ternary complex does not support the assumption, that this occurs by simply the 6-TG molecule replacing DMSO molecule at both sites. One explanation is that 6-TG molecule is bound to the multiple sites of the A100 host material in a complicated fashion. Another explanation could be that the A100 has a higher affinity for DMSO molecule, and the current encapsulation procedure is not suitable for every DMSO to be displaced by the 6-TG molecule.

3.2.9 Investigation of fine band gap changes between A100 and A100-DMSO

Optical band gaps of MOFs have typically been measured by the UV-Vis DRS method[62], a technique with the disadvantage that it determines the band gap through the extrapolation methods (using the side of a spectral curve) and not directly from the maximum of a specific peak. Determining an optical band gap by this method results in the large variety of reported results for the same band gap of the same MOF[63]. Band gaps have been determined for other solids using the conventional photoluminescence spectroscopy[64]. However, the synchronous fluorescence spectroscopy has yet to be used for analysis of the solid-state materials, and particularly MOFs. As the synchronous fluorescence experiments depend strongly on the monochromaticity of the excitation and emission light (with any deviations meaning that the emission and excitation would no longer be synchronized), the monochromator slit width was gradually decreased in this work from the default value of 5 nm to gain an additional accuracy. While the slit width reduction from 5 nm down to 1 nm have produced the significant narrowing of spectral peaks, a reduction to 1 nm has drastically lowered the overall detected signal strongly enough, so that the signal-to-noise ratio (S/N) became unacceptably low. All further band gap investigations were performed with an excitation and emission slit width of 2 nm, Figure 30.

For the binary complex A100-DMSO, the emission caused by absorption of light around 345 nm is the strongest within the $\Delta\lambda$ = 50-58 nm. Since the optical band gap in MIL-53(Al), which is similar to Basolite A100, was reported at 3.56 eV (348 nm)[47] we

can assume that the peak maximum at 345 nm corresponds to absorption across the band gap in A100. For larger Δλ = 80-88 nm, the emission due to absorption at 308 nm is the strongest. This corresponds to the absorption resonance of the individual BDC linker in A100. Additionally, it is important to note that the variable Δλ is expected to occasionally match the Stokes shift (the difference between the wavelength of the emission and excitation photons of a given fluorophore), and the smaller Δλ allows for a greater possibility of matching the Stokes shift exactly. When this occurs, the corresponding transition achieves high intensity and sharp peak shape. These advantages are important for accurate determination of numeric values of band gaps.

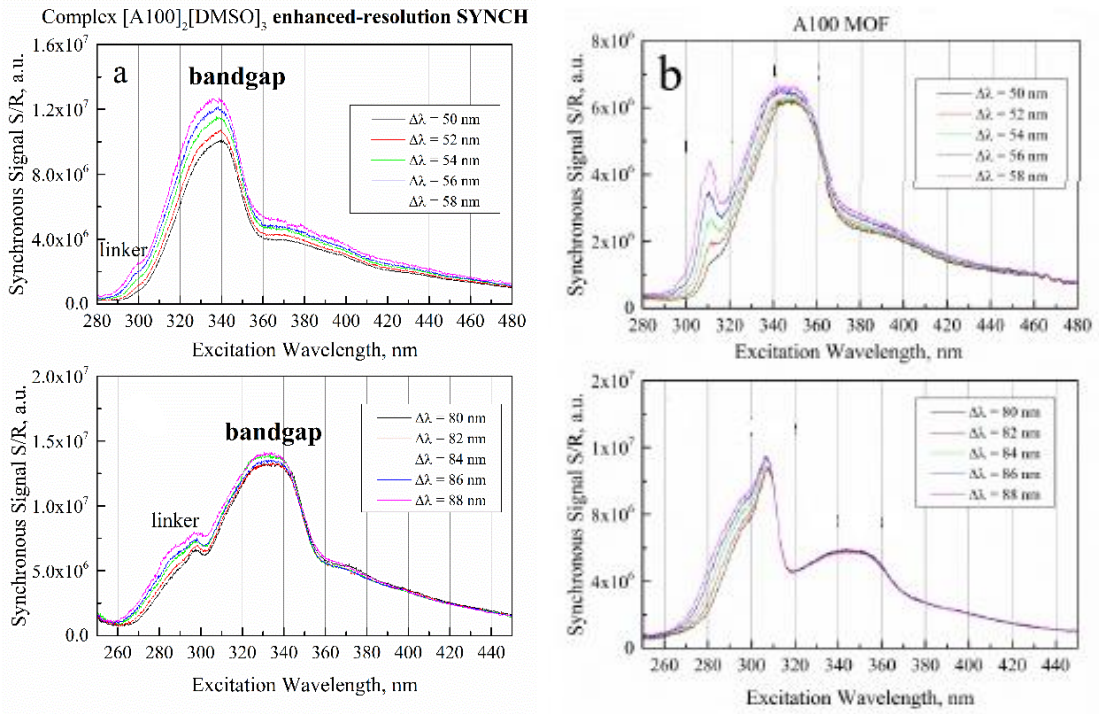

Figure 30a,b. Comparing synchronous fluorescence spectra of A100 and A100-DMSO at small Δλ

As discussed in section 3.2.6, the peaks due to both the BDC linker and the band gap have been blue-shifted in the spectra of the binary complex as compared to that of A100. This resulted in an increase of its band gap relative to that of A100. This increase in band gap should be due to either a) the increase of energy of the conduction band (CB), which corresponds to the lowest unoccupied molecular orbital (LUMO) in the molecules or b) decrease of energy of the valence band (VB) which corresponds to the highest occupied molecular orbital (HOMO). For this to occur, either the CB was destabilized, or the VB stabilized when A100 absorbs DMSO molecules. Since the VB is formed by the filled electronic states of the π-system of the BDC linker and thus serves as an elector donor, stabilization could occur by the interaction with an electron acceptor. Of the two guest molecules under consideration in this study, DMSO would serve as a better electron acceptor than 6-TG, so any shift in the band gap should be due to its interaction with A100.

$\Delta\lambda$, nm	**50**	**52**	**54**	**56**	**58**
λ_{em} of actA100, nm	346.8	346.2	345.7	345.1	344.6
E_g of actA100, eV	3.576	3.582	3.587	3.593	3.598

Table 1. Band gap energy E_g of the activated Basolite A100 from the solid-state enhanced-resolution synchronous fluorescence (excitation) spectra

Tables 1 and 2 list values of band gaps and energies of optical transitions in Basolite A100 as determined from the spectra at low $\Delta\lambda$, which are based on Gaussian fitting of the 340-345 nm peaks. This fitting does not include any neighboring spectral shoulders.

Δλ, nm	**80**	**82**	**84**	**86**	**88**
λ_{em} of complex $[A100]_2[DMSO]_3$, nm	336.2	335.7	335.3	334.9	334.3
Eg of complex $[A100]_2[DMSO]_3$, eV	3.688	3.694	3.698	3.703	3.709

Table 2. Band gap energy E_g of the $[A100]_2[DMSO]_3$ from the solid-state enhanced-resolution synchronous fluorescence spectra

Since the presence of 6-TG molecule did not appear to affect the position of the band gap in the ternary complex relative to that of the binary complex, its values were not calculated here.

It is notable to see how consistent the difference is between band gaps of A100 and A100-DMSO across the range of different Δλ. While the difference of the band gap energies is 0.112 eV for Δλ = 50 nm, for instance at Δλ = 58 nm it remains nearly constant at 0.111 eV. At the same time, the dependence of the E_g on Δλ of the either material is very weak. For both A100 and the binary complex, the difference between the low Δλ at 50 nm and the high Δλ at 58 nm is as small as 0.02 eV.

3.3 Release of 6-TG drug

3.3.1 Release of 6-TG from powder of A100-DMSO-6TG

The change of molar concentration of 6-TG released from A100-DMSO-6TG in physical form of powder in PBS versus the release time (kinetics) is shown in Figure 31.

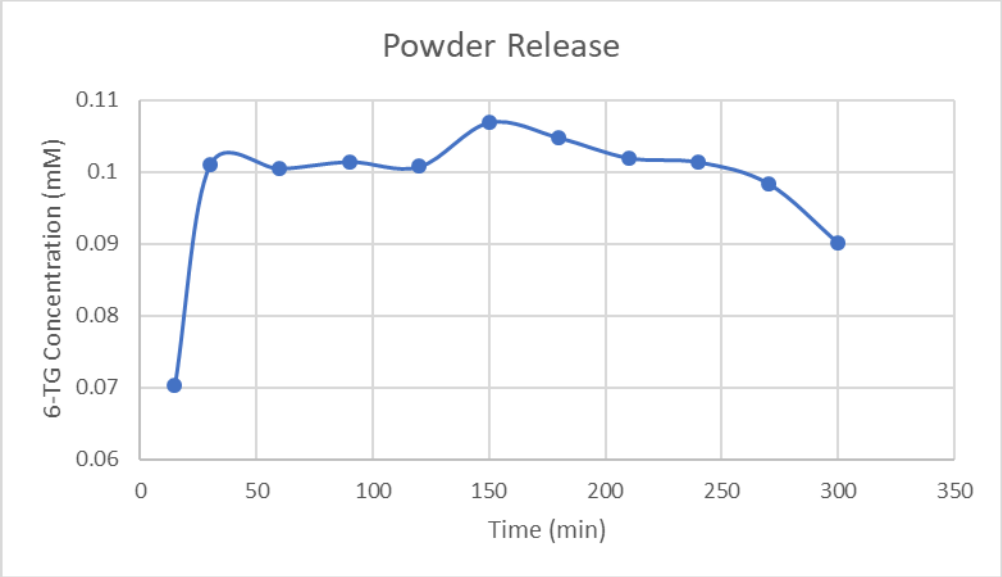

Figure 31. Kinetics of release of 6-TG from the ternary complex as powder to PBS

As a reference experiment, an amount of pure powdered 6-TG was analyzed under the same conditions and sampling regimen as the powdered ternary complex (Figure 32, labeled as “hydrolysis”). The amount of 6-TG in the reference sample was the same as the amount of 6-TG in the ternary complex, for consistency.

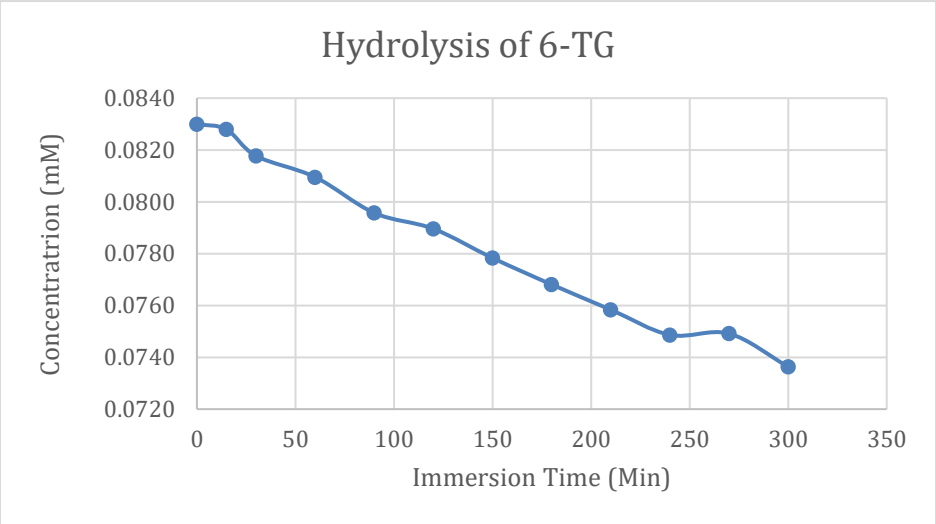

Figure 32. Kinetics of release of 6-TG as powder to PBS

For the drug release from the powdered ternary complex, a few key features are notable. As this release is cumulative (the released 6-TG accumulates in the PBS solution), there is a "burst" in the first 30 minutes, when a large amount of 6-TG moves in to the buffer. Once this initial "burst" release occurs, the concentration remains steady for few hours with no additional 6-TG appearing in the PBS. After 2 hours, however, an additional incremental increase occurs, followed by a slow decline whose pace is increased toward the end of the experiment. Looking at the reference curve for 6-TG in under the same conditions (Figure 32), a steady decrease in concentration is observed over the entire time period. This indicates that, independently of any biological metabolic processes, 6-TG in PBS at pH 3.7 at 37 ˚C seem to gradually degrade to compounds which do not absorb at 345 nm (the monitoring wavelength of the HPLC-UV experiment). This also suggests that the plateau after 60 min. is not a pause in release, but rather a slow release at roughly the same rate as the process of decomposition the 6-TG molecule. Additionally, the small increase in concentration at 150 min. is not the start of

a release, but the first time when the release rate was larger than the rate of decomposition of 6-TG (possibly by hydrolysis and/or oxidation).

An initial quick release was followed by a slower release. This is consistent with the idea proposed during sample characterization, that there are two kinds of guest molecules in the complex of A100. The initial fast release could correlate with 6-TG molecules bound to the sites other than the linker and the non-breathing related sorption site. The subsequent release (after the "burst") is correlated to those 6-TG molecules which are bound to the BDC linker. However, due to the overall fast release and overall low concentration of the 6-TG, there is a risk of extrapolating too far from very small changes in the concentration over the frequent sampling intervals (which required maintaining the constant PBS volume in the release flask). Pelletizing both the sample and the reference and suspending them in a much smaller volume of PBS would address both issues.

3.3.2 Release of 6-TG from A100-DMSO-6TG pellet

Many features of drug release from the ternary complex in the form of powder are observed in the release kinetics of the complex in the pellet form, Figure 33. The initial "burst" release is still present, and the rate of release during the "burst" by the pelletized sample is close to that of the pelletized pure 6-TG (orange line, Figure 33). This suggests that the non-linker bound 6-TG is weakly bound to its site, as it moves into the solution at, roughly, the same rate as 6-TG molecules bound to other 6-TG molecules in the 6-TG pellet. A plateau is seen in the pellet of the complex around 500 min. that is not present in the release of the pellet of pure 6-TG. It's important to note that both samples cracked

half way through the first day, which likely explains the sharp peaks seen before this time point. More surface area became available for dissolution at this time point, explaining the increase in the rate of release. After this plateau, another increase in the concentration is seen in Figure 33 for both samples. As this increase is observed for both the sample pellet and the reference pellet, it is likely related to the increase in the sampling interval. Namely, after the first full 12 hours, the sampling interval was switched to once every 12 hours which allowed more 6-TG to accumulate in the PBS (per sampling interval).

Then, the rate of release declines in the 2100-2500 min. range for both the pelletized sample and the reference, suggesting that this is an artifact of sample preparation and/or release procedure, and is not directly related to binding 6-TG molecule. One explanation is that these peaks occurred after the first 12 hour residence time in the PBS. These longer exposure times let the buffer solution fully penetrate inside both pellets for the first time, allowing the PBS access to the 6-TG molecules that had been more protected inside the pellet initially. Upon the subsequent release intervals, these non-linker bound molecules were already released, thus leading to a comparatively lower concentration of the newly released 6-TG. This process occurred faster for the ternary complex than for the 6-TG reference material.

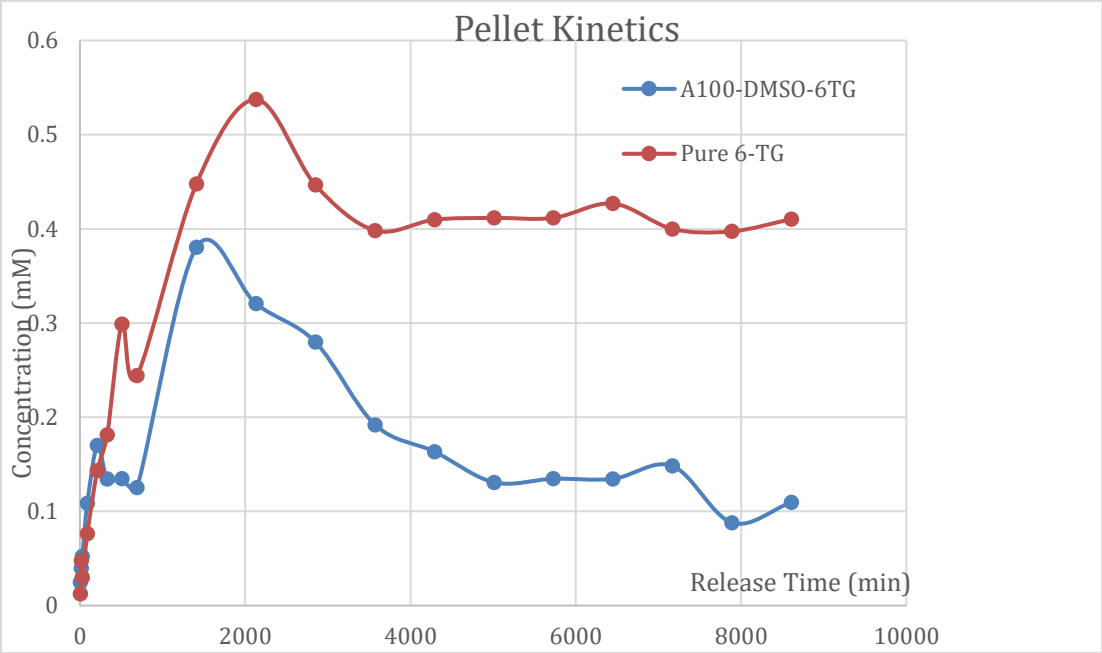

Figure 33. Release profile of 6-TG from pellet of A100-DMSO-6TG and pure 6-TG pellet

After this point, the concentration of 6-TG released from the reference (the pellet of pure 6-TG) and the sample (the complex) began to differ more noticeably. The 6-TG concentration for the reference reaches the plateau after decreasing, which was expected[65]. With no additional penetration of PBS (and thus release of additional 6-TG from the interior of the pellet) and with each sampling occurring at the equal time interval (starting when the pellet is transferred to fresh PBS), the amount of 6-TG released to the buffer should be relatively constant for most of the time, as observed. However, for the ternary complex, the rate of 6-TG release to PBS slows down over the subsequent day's samplings. This suggests there is a force not related to the pelletizing that is inhibiting the movement of 6-TG molecules to the buffer. These are the 6-TG molecules that are bound to the linker in the A100. The bonding energy due to the π-π stacking is likely slowing

down the release when compared to both the pure 6-TG (which is constant) and the earlier release from the complex (which was considerably faster). The molecule of 6-TG seems to occupy both some not linker-related “fast-releasing” site and a linker-related “slow-releasing” site. Also, while pellets of both the reference (pure 6-TG) and the sample (ternary complex) started to release roughly the same amount of 6-TG per unit volume of PBS, over the week the pellet of the ternary complex a) has released the lower amount of 6-TG total vs. the reference and b) has released that amount at the slower rate. In terms of the time-delayed drug release as one of goal of this study, the ternary complex has shown to significantly delay the release of 6-TG to the PBS as a simulated biological fluid.

4 Conclusion

Gravimetric studies have shown the encapsulation complexes of A100 to be $[A100]_2[DMSO]_3$ and $[A100]_2[DMSO]_3[6\text{-}TG]_1$. For the binary complex A100-DMSO, the encapsulated DMSO was found to be located either on the BDC linker, or on an -OH group on an Al atom. For a given unit cell of A100, this bonding corresponds to a stoichiometry of $[A100]_2[DMSO]_3$. For the ternary complex A100-DMSO-6TG, the 6-TG was found to bind to the organic linker and to displace the DMSO in doing so. It is uncertain as to whether any 6-TG binds to the -OH group on the Al atom. However, the ternary complex' stoichiometry $[A100]_2[DMSO]_3[6\text{-}TG]_1$ does suggest a more complicated scheme than one 6-TG molecule bound to one linker per A100 unit.

Release studies suggest the existence of two differently bound 6-TG molecules: one that is fast releasing and another that is slow releasing. The 6-TG molecule attached to the linker should be more strongly bound due to the additional π- π stacking present, and 6-TG molecule bound here was slower releasing. The 6-TG molecule bound to the -OH location accounts for the more quickly occurring release, as the bonds there are weaker.

The research of pelletizing also shows that even without binder, the compressed sample of ternary complex will release their drug slower than pure 6-TG reference. This shows its potential of surviving metabolic processes with its drug payload intact. It also shows promise as a means of releasing drugs at a specific body site over an extended period via implantation. This would be suitable for some kinds of cancer growth suppression techniques already used for "after-care" of post-removal surgery sites. While

it may require additional interpretation, the sampling method for the pelletized drug release shows advantages over the traditional method of sampling one solution over the course of an experiment. The “instantaneous” rate comparisons between the reference and sample offer information, which is otherwise concealed due to having to take rate averages over the entire sampling time and concentration.

Finally, MDSC and solid-state synchronous fluorescence spectroscopy were shown to offer improvements from their respective conventional analytical methods. Synchronous fluorescence spectra showed a great deal more resolution, allowing to calculate peaks due to the monomer and excimer that allowed the determination of the band gap (and its changes) and behavior of the linker that was obscured in the conventional spectra. And the ability to differentiate between the reversible and irreversible endothermic processes is helpful in identifying the more specific behavior of adsorbed molecules. The ability to determine the reversible heat flow was key in finding the “breathing” behavior that otherwise would have been obscured by strong absorption/desorption processes.

4.1 Future studies

There are several avenues for future study to build off the work presented here. The characterization could be improved by IR spectroscopy e.g. DRIFTS, which could help determine which IR peaks are impacted after encapsulation and thus where the guest molecules are located. Long-term release studies of the pelletized sample on cancer cell lines could help prove the benefits of MOF encapsulated drugs in having good stability for implantation purposes, and more pelletizing research e.g. the addition of binders

could also help in this area. Relatedly, as 6-TG is currently mostly an oral medication, powder release studies in more acidic media would be useful in determining if the A100 is protecting the 6-TG in this harsh environment enough that a viable concentration remains after certain time scale. Also, longer and more advanced encapsulation techniques should be tested to see what effect they have on the ternary complex's stoichiometry. Lastly, the characterization methods developed here could do well to determine encapsulation in other MOF-drug systems, particularly those encapsulated by one-pot means where accurate gravimetric determination is even more difficult. As one-pot methods are very useful in encapsulating the larger molecules such as enzymes, that are at the leading edge of anti-cancer therapies, characterization methods suiting to support those kinds of encapsulations would be useful in allowing MOFs to stay apace with biomedical advancement.

References

(1) D. W. Beck, *Zeolite Molecular Sieves*, John Wiley and Son, New York, **1974**, 771 pp.

(2) L. Huang, H. Wang, J. Chen, Z. Wang, J. Sun, D. Zhao and Y. Yan, *Microporous Mesoporous Mater.* **2003**, *58*, 105-114.

(3) N. L. Rosi, J. Eckert, M. Eddaoudi, D. T. Vodak, J. Kim, M. O'Keeffe and O. M. Yaghi, *Science* **2003**, *300*, 1127-1129.

(4) H. K. Chae, D. Y. Siberio-Perez, J. Kim, Y. Go, M. Eddaoudi, A. J. Matzger, M. O'Keeffe and O. M. Yaghi, *Nature* **2004**, *427*, 523-527.

(5) C. Janiak and J. K. Vieth, *New J. Chem.* **2010**, *34*, 2366-2388.

(6) V. Agostoni, R. Anand, S. Monti, S. Hall, G. Maurin, P. Horcajada, C. Serre, K. Bouchemal and R. Gref, *J. Mater. Chem. B* **2013**, *1*, 4231-4242.

(7) Q. R. Fang, G. S. Zhu, M. Xue, Q. L. Zhang, J. Y. Sun, X. D. Guo, S. L. Qiu, S. T. Xu, P. Wang, D. J. Wang and Y. Wei, *Chem. Eur. J.* **2006**, *12*, 3754-3758.

(8) Q. Y. Li, S. F. Ji and Z. M. Hao, *Prog. Chem.* **2012**, *24*, 1506-1518.

(9) P. S. Wheatley, A. R. Butler, M. S. Crane, A. G. Rossi, I. L. Megson, R. E. Morris, J. Cejka, N. Zilkova and P. Nachtigall, *Molecular Sieves: from Basic Research to Industrial Applications, Parts A and B*, **2005**, p. 2033.

(10) H.-C. Zhou, D. Feng and K. Wang, *Patent US 9102691 B2*.

(11) J. R. Li, J. Sculley and H. C. Zhou, *Chem. Rev.* **2012**, *112*, 869-932.

(12) L. Bromberg, Y. Klichko, E. P. Chang, S. Speakman, C. M. Straut, E. Wilusz and T. A. Hatton, *ACS Appl. Mater. Interfaces* **2012**, *4*, 4595-4602.

(13) H. L. Jiang and Q. Xu, *Chem. Commun.* **2011**, *47*, 3351-3370.

(14) J. Mollmer, M. Lange, A. Moller, C. Patzschke, K. Stein, D. Lassig, J. Lincke, R. Glaser, H. Krautscheid and R. Staudt, *J. Mater. Chem.* **2012**, *22*, 10274-10286.

(15) U. Mueller, M. Schubert, F. Teich, H. Puetter, K. Schierle-Arndt and J. Pastre, *J. Mater. Chem.***2006**, *16*, 626-636.

(16) A. U. Czaja, N. Trukhan and U. Muller, *Chem. Soc. Rev.* **2009**, *38*, 1284-1293.

(17) P. Horcajada, C. Serre, M. Vallet-Regí, M. Sebban, F. Taulelle and G. Férey, *Angew. Chem. Int. Ed.* **2006**, *45*, 5974-5978.

(18) A. Sonnauer, F. Hoffmann, M. Froba, L. Kienle, V. Duppel, M. Thommes, C. Serre, G. Ferey and N. Stock, *Angew. Chem. Int. Ed.* **2009**, *48*, 3791-3794.

(19) P. Horcajada, C. Serre, G. Maurin, N. A. Ramsahye, F. Balas, M. Vallet-Regi, M. Sebban, F. Taulelle and G. Ferey, *J. Am. Chem. Soc.* **2008**, *130*, 6774-6780.

(20) K. M. L. Taylor-Pashow, J. D. Rocca, Z. Xie, S. Tran and W. Lin, *J. Am. Chem. Soc.* **2009**, *131*, 14261-14263.

(21) B. Lei, M. Wang, Z. Jiang, W. Qi, R. Su and Z. He, *ACS Appl. Mater. Interfaces* **2018**, *10*, 16698-16706.

(22) R. Liu, T. Yu, Z. Shi and Z. Wang, *Int. J. Nanomed.* **2016**, *11*, 1187.

(23) S. H. Jang, M. G. Wientjes, D. Lu and J. L. Au, *Pharm Res* **2003**, *20*, 1337-1350.

(24) R. C. Huxford, J. Della Rocca and W. Lin, *Curr. Opin. Chem. Biol.* **2010**, *14*, 262-268.

(25) C. E. Bugg and U. Thewalt, *J. Am. Chem. Soc.* **1970**, *92*, 7441-7445.

(26) H. M. Aliabadi, M. Romanick, V. Somayaji, P. Mahdipoor and A. Lavasanifar, *American Journal of Health-System Pharmacy* **2011**, *68*, 900-908.

(27) Y. V. Rubin, *XVI International Conference on Spectroscopy of Molecules and Crystals* **2004**, p. 12.

(28) P. N. Munshi, M. Lubin and J. R. Bertino, *Oncologist* **2014**, *19*, 760–765.

(29) Z. Hasan and S. H. Jhung, *J. Hazard. Mater.* **2015**, *283*, 329-339.

(30) K. M. Park, H. Kim, J. Murray, J. Koo and K. Kim, *Supramol. Chem.* **2017**, *29*, 441-445.

(31) S. Y. Jia, Y. F. Zhang, Y. Liu, F. X. Qin, H. T. Ren and S. H. Wu, *J. Hazard. Mater.* **2013**, *262*, 589-597.

(32) D. Cunha, M. Ben Yahia, S. Hall, S. R. Miller, H. Chevreau, E. Elkaim, G. Maurin, P. Horcajada and C. Serre, *Chem. Mater.* **2013**, *25*, 2767-2776.

(33) K. Capriotti and J. A. Capriotti, *J. Clin. Aesthet. Dermatol.* **2012**, *5*, 24-26.

(34) A. Nalaparaju and J. Jiang, *Langmuir* **2012**, *28*, 15305-15312.

(35) F. M. Hinterholzinger, B. Ruhle, S. Wuttke, K. Karaghiosoff and T. Bein, *Scientific Reports* **2013**, *3*.

(36) J. B. Wolinsky, Y. L. Colson and M. W. Grinstaff, *J. Control. Release* **2012**, *159*, 14-26.

(37) G. Ferey and C. Serre, *Chem. Soc. Rev.* **2009**, *38*, 1380-1399.

(38) W. P. Mounfield and K. S. Walton, *J. Colloid Interface Sci.* **2015**, *447*, 33-39.

(39) S. K. Elsaidi, M. H. Mohamed, D. Banerjee and P. K. Thallapally, *Coord. Chem. Rev.* **2018**, *358*, 125-152.

(40) N. A. Khan, Z. Hasan and S. H. Jhung, *J. Hazard. Mater.* **2013**, *244*, 444-456.

(41) A. E. J. Hoffman, L. Vanduyfhuys, I. Nevjestić, J. Wieme, S. M. J. Rogge, H. Depauw, P. Van Der Voort, H. Vrielinck and V. Van Speybroeck, *J. Phys. Chem. C* **2018**, *122*, 2734-2746.

(42) S. Ling and B. Slater, *J. Phys. Chem. C* **2015**, *119*, 16667-16677.

(43) S. Devautour-Vinot, G. Maurin, F. Henn, C. Serre, T. Devic and G. Férey, *Chem. Commun.* **2009**, 2733-2735.

(44) S. Rubio, A. Gomez-Hens and M. Valcarcel, *Talanta* **1986**, *33*, 633-640.

(45) F. Capitán, G. Sánchez-Palencia, A. Navalón, L. Fermín Capitán-Vallvey and J. Luis Vilchez, *Anal. Chim. Acta* **1992**, *259*, 345-353.

(46) Q. Liu, K. Chen, M. Martin, A. Wintenberg, R. Lenarduzzi, M. Panjehpour, B. F. Overholt and T. Vo-Dinh, *Opt. Express* **2007**, *15*, 12583-12594.

(47) C.-X. Yang, H.-B. Ren and X.-P. Yan, *Anal. Chem.* **2013**, *85*, 7441-7446.

(48) A. Saha and D. Strickland, *J. Therm. Anal. Calorim.* **2016**, *126*, 1747-1755.

(49) L. C. Thomas, *TA Technical Papers* **2005**, *T006*, 8.

(50) D. Wu and A. Navrotsky, *J. Solid State Chem.* **2015**, *223*, 53-58.

(51) A. Samokhvalov, *Coord. Chem. Rev.* **2018**, *374*, 236-253.

(52) P. A. Andrews, M. J. Egorin, M. E. May and N. R. Bachur, *J. Chromatogr. B* **1982**, *227*, 83-91.

(53) J. Dai, M. L. McKee and A. Samokhvalov, *J. Phys. Chem. C* **2015**, *119*, 2491-2502.

(54) M. Yu, Z. Li, Q. Xia, H. Xi and S. Wang, *Chem. Eng. J.* **2007**, *132*, 233-239.

(55) F. Salles, G. Maurin, C. Serre, P. L. Llewellyn, C. Knöfel, H. J. Choi, Y. Filinchuk, L. Oliviero, A. Vimont, J. R. Long and G. Férey, *J. Am. Chem. Soc.* **2010**, *132*, 13782-13788.

(56) X. K. Qian, B. L. Yadian, R. B. Wu, Y. Long, K. Zhou, B. Zhu and Y. Z. Huang, *Int. J. Hydrogen Energy* **2013**, *38*, 16710-16715.

(57) G. Ortiz, G. Chaplais, J.-L. Paillaud, H. Nouali, J. Patarin, J. Raya and C. Marichal, *J. Phys. Chem. C* **2014**, *118*, 22021-22029.

(58) G. S. Abdrakhimova, M. Y. Ovchinnikov, A. N. Lobov, L. V. Spirikhin, S. P. Ivanov and S. L. Khursan, *J. Phys. Org. Chem.* **2014**, *27*, 876-883.

(59) S. R. Gardner, L. M. Selby, R. K. Teranishi, M. S. Douglas, S. W. Simonds, K. A. Martin and A. M. Nishimura, *J. Lumin.* **2013**, *134*, 657-664.

(60) M. Alvaro, E. Carbonell, B. Ferrer, F. Xamena and H. Garcia, *Chem. Eur. J.* **2007**, *13*, 5106-5112.

(61) C. Grinnell and A. Samokhvalov, *Phys. Chem. Chem. Phys.* **2018**, *20*, 26947-26956.

(62) P. Dhage, A. Samokhvalov, M. L. McKee, E. C. Duin and B. J. Tatarchuk, *Surf. Interf. Anal.* **2013**, *45*, 865-872.

(63) M. L. Myrick, M. N. Simcock, M. Baranowski, H. Brooke, S. L. Morgan and J. N. McCutcheon, *Appl. Spectrosc. Rev.* **2011**, *46*, 140-165.

(64) B. Monemar, *Phys. Rev. B* **1974**, *10*, 676-681.

(65) *In-Situ Spectroscopy in Heterogeneous Catalysis*, Wiley-VCH, Weinheim, **2002**, 276 pp.